Chair of Materials Science and Testing of Polymers

Master's Thesis

# Delamination resistance testing of fiber reinforced polymer laminates combined with acoustic emission analysis

Veronika Koss, BSc

September 2023

**MONTANUNIVERSITÄT LEOBEN**
www.unileoben.ac.at

## EIDESSTATTLICHE ERKLÄRUNG

Ich erkläre an Eides statt, dass ich diese Arbeit selbständig verfasst, andere als die angegebenen Quellen und Hilfsmittel nicht benutzt, und mich auch sonst keiner unerlaubten Hilfsmittel bedient habe.

Ich erkläre, dass ich die Richtlinien des Senats der Montanuniversität Leoben zu "Gute wissenschaftliche Praxis" gelesen, verstanden und befolgt habe.

Weiters erkläre ich, dass die elektronische und gedruckte Version der eingereichten wissenschaftlichen Abschlussarbeit formal und inhaltlich identisch sind.

Datum 09.09.2023

V Koss

Unterschrift Verfasser/in
Veronika Koss

# ACKNOWLEDGEMENT

I would like to take this opportunity to thank everyone who supported me during the process of this thesis.

First of all, I would like to express my gratitude to Univ.-Prof. Dipl.-Ing. Dr.mont. Gerald Pinter, head of the Chair of Materials Science and Testing of Polymers at Montanuniversität Leoben, for the opportunity to write this thesis at this Chair and for reviewing my thesis.

I would like to express by deepest gratitude to my supervisor Dipl.-Ing. Maria Gfrerrer for her ongoing support and help during the process my work. Without her guidance and persistent help this thesis would not have been possible. Special thanks also go to Dipl.-Ing. Dr.mont. Johannes Wiener, for his support and sharing of his knowledge. Furthermore, my deepest appreciation goes to Dr. Andreas Brunner from the Swiss Federal Laboratories for Materials Testing and Research, who was always open to give feedback and help when needed. I am also thankful to Jürgen Grosser for the introduction of the machines and his help changing the test configurations many times.

Lastly, I would be remiss in not mentioning my family and friends, who supported me during my studies. Special thanks go to my parents, without their support this would have not been possible. Many thanks also go to Patrick, for his ongoing support and always finding ways to cheer me up during our time in Leoben.

# ABSTRACT

Fiber reinforced polymers are used in a wide variety of applications, especially in light weight applications where high stiffness and strength are required while maintaining low weight. Since delamination often occurs in fiber reinforced polymers and can result in the failure of the component, it is important to gain deep insight into their fracture mechanical behavior. It is still state of the art to observe the growing crack length with a microscope or camera system and manually determine the initiation and propagation of the crack, which can lead to subjective and inaccurate results. The use of acoustic emission (AE) analysis could be a solution to automate the crack initiation and crack length detection.

The aim of this thesis was to determine the delamination behavior of glass fiber (GFRP) and carbon fiber reinforced polymer (CFRP) laminates with the same epoxy matrix system. For this purpose, the critical energy release rate was determined for both materials with different test setups. Mode I, mode II and mixed mode I/II tests were performed according to different standard methods. For mode II and mixed mode I/II two standard methods were tested in order to compare the results to each other. To gain a deeper insight into the delamination behavior, a special focus was given to the method of AE. The crack initiation was determined by the use of AE and compared to the initiation values according to standard methods. Furthermore, AE was used to perform a localization of the crack front. The detected crack front via AE was compared to the results of the visually observed crack front. Microscopy was performed for all specimen in order to gain insights into differences of fracture surfaces depending on the loading mode.

The determined critical energy release rates for all tested modes showed similar trends for both materials. Mode I tests resulted in the lowest values for the critical release rate, followed by mixed mode I/II tests and the highest values were measured during mode II testing. The initiation values were lower than the propagation values and the onset obtained with AE resulted in the most conservative initiation criterion. It was shown that AE can be used to determine the onset of delamination. The critical energy release rate for GFRP was approximately two times higher than for CFRP.

The analysis of the fracture surfaces showed differences depending on the tested mode. The surfaces of mode II and mixed mode I/II tested specimens showed shear hackles, which are typical for mode II fracture surfaces. Surfaces of mode I tested specimens did not show any sign of shear forces, but evenly distributed fibers with no loose matrix material in between.

The localization of the crack front via AE yielded good results, which were in accordance with the detected crack front via the camera system. The localization of the AE signals showed a band with high amplitude AE signals. For mode I tests, this band was wider distributed for GFRP which is a sign for fiber bridging, which could be observed during the tests as well. This fact could be seen in the increasing resistance curve of mode I GFRP tests as well. Another reason for the wider distributed AE signals for GFRP laminates is that due to the lower velocity of sound of GFRP compared to CFRP the localization is less accurate and leads to more scattering of the results.

In conclusion, all tested methods yielded reasonable results and both materials showed the same trends. It was shown that AE can be used as a helpful method for the investigation of the delamination behavior of composite materials.

# KURZFASSUNG

Faserverstärkte Kunststoffe finden in einer Vielzahl an Anwendungen ihren Einsatz, vor allem in Leichtbauanwendungen, bei denen hohe Steifigkeiten und Festigkeiten bei geringem Gewicht von großer Bedeutung sind. Delamination tritt bei Laminaten häufig auf und kann zum Versagen führen, daher ist es von großer Bedeutung das bruchmechanische Verhalten von faserverstärkten Kunststoffen zu kennen. Nach dem Stand der Technik, wird die Rissinitiierung und der Risslängenfortschritt mit einem Mikroskop oder Kamerasystem beobachtet und so die Rissentstehung und Ausbreitung manuell bestimmt. Dies führt allerdings zu subjektiven und ungenauen Ergebnisse. Der Einsatz der Schallemissionsanalyse (AE) könnte eine Lösung sein, um die Bestimmung der Rissinitiierung und Risslänge zu automatisieren.

Ziel dieser Arbeit war es das Delaminationsverhalten von glasfaser- (GFK) und carbonfaserverstärkte Kunststofflaminaten (CFK) mit demselben Epoxidmatrixsystem zu bestimmen. Es wurde die kritische Energiefreisetzungsrate für beide Materialien in verschiedenen Versuchsaufbauten bestimmt. Tests für Mode I, II und Mixed Mode I/II Belastung wurden nach verschiedenen Normen durchgeführt. Für Mode II und Mixed Mode I/II wurde jeweils nach zwei Normen getestet, um die Ergebnisse miteinander zu vergleichen. Um einen tieferen Einblick in das Delaminationsverhalten von Verbundwerkstoffen zu erhalten, wurde des Weiteren der Fokus auf die Schallemissionsanalyse gelegt. Mithilfe der Schallemissionsanalyse wurde die Rissinitiierung bestimmt und mit den Werten der Standardmethoden verglichen. Darüber hinaus wurde die Schallemissionsanalyse dazu verwendet, die Rissfront zu lokalisieren. Der so ermittelte Rissfortschritt wurde mit der visuell beobachteten Rissfront verglichen. Durch mikroskopische Untersuchungen wurden die Bruchflächen aller Proben dahingehend untersucht, ob es Unterschiede abhängig des getesteten Modes gibt.

Die ermittelten kritischen Energiefreisetzungsraten für alle getesteten Versuchsaufbauten zeigten für beide Materialien ähnliche Trends. Die niedrigsten Werte ergaben sich bei den Mode I Prüfungen, gefolgt von den Mixed Mode I/II Prüfungen. Die höchsten Werte wurden bei Mode II Prüfungen ermittelt. Die Energiefreisetzungsraten der Rissinitiierung ergaben jeweils niedrigere Werte als die der Rissausbreitung. Die Initiierungswerte, die

mithilfe der Schallemissionsanalyse ermittelt wurden, ergaben die konservativsten Ergebnisse. Es konnte gezeigt werden, dass die Schallemissionsanalyse eine brauchbare Methode ist, um den Beginn der Delamination zu bestimmen. Die kritische Energiefreisetzungsrate für das GFK-Laminat war ungefähr doppelt so hoch wie für das CFK-Laminat.

Die mikroskopische Analyse der Bruchflächen zeigte Unterschiede abhängig vom geprüften Mode. Die Bruchflächen der Mode II und Mixed Mode I/II geprüften Proben wiesen die für diesen Mode typischen „shear hackles“ auf. Die Bruchflächen der Mode I geprüften Prüfkörper zeigten keine Anzeichen von Scherung, aber es konnten gleichmäßig verteilte Fasern mit Matrixmaterial dazwischen festgestellt werden.

Die Rissfrontlokalisierung mittels Schallemissionsanalyse konnte ebenfalls gute Ergebnisse liefern, die mit dem optisch erfassten Rissfrontfortschritt übereinstimmen. Die Lokalisierung der akustischen Signale zeigte ein Band mit den hochenergetischen Signalen. Bei Mode I Versuchen der GFK-Laminate war dieses Band breiter ausgeprägt als für die CFK-Laminate, was auf „fiber bridging“ zurückzuführen ist, welches bei GFK stärker zu beobachten war als bei CFK. Dies zeigt sich auch in der R-Kurve der Mode I Versuche von GFK, welche im Gegensatz zu CFK kein Plateau bildet. Ein weiterer Grund für die stärkere Streuung der GFK-Laminaten könnte die niedrigere Schallgeschwindigkeit im Vergleich zu CFK sein, da es bei niedrigeren Schallgeschwindigkeiten zu einer ungenaueren Signalordnung kommt.

Zusammenfassend kann gesagt werden, dass alle getesteten Methoden zu vernünftigen Ergebnissen führten und bei beiden Materialien die gleichen Trends festgestellt werden konnten. Es konnte gezeigt werden, dass die Schallemissionsanalyse eine hilfreiche Methode ist, um das Delaminationsverhalten von Verbundwerkstoffen zu bestimmen.

# TABLE OF CONTENT

**SYMBOLS** ..... **1**

**LIST OF FIGURES** ..... **3**

**LIST OF TABLES** ..... **7**

**1 INTRODUCTION** ..... **8**

**2 THEORETICAL BACKGROUND** ..... **10**

2.1 Delamination of composites ..... 10

2.1.1 Linear Elastic Fracture Mechanics ..... 12

2.1.2 Norms / Standards ..... 15

2.2 Acoustic Emission ..... 16

2.2.1 Principle ..... 17

2.2.2 Analysis of Acoustic Emission signals ..... 18

2.2.3 Source Localization ..... 20

2.2.4 Application to Delamination Resistance Testing of FRP Laminates ..... 21

**3 EXPERIMENTAL** ..... **23**

3.1 Materials and Specimens ..... 23

3.2 Setup ..... 25

3.3 Procedure ..... 27

3.3.1 Acoustic Emission ..... 27

3.3.2 Optical evaluation ..... 28

3.4 Evaluation of fracture mechanical parameters ..... 28

3.4.1 Evaluation of delamination initiation ..... 28

3.4.2 Evaluation of delamination propagation ..... 30

**4 RESULTS** ..... **31**

4.1 Glass fiber reinforced polymer ..... 31
4.1.1 Mode I – DCB ..... 31
4.1.2 Mode II – ELS ..... 33
4.1.3 Mode II – ENF ..... 35
4.1.4 Mixed mode I/II – FRMM ..... 36
4.1.5 Mixed mode I/II – MMB ..... 38
4.1.6 Fracture surfaces ..... 39
4.1.7 Summary of GFRP results ..... 41
4.2 Carbon fiber reinforced polymer ..... 42
4.2.1 Mode I – DCB ..... 42
4.2.2 Mode II – ELS ..... 44
4.2.3 Mode II – ENF ..... 46
4.2.4 Mixed mode I/II – FRMM ..... 46
4.2.5 Mixed mode I/II – MMB ..... 48
4.2.6 Fracture surfaces ..... 49
4.2.7 Summary of CFRP results ..... 51
4.3 Comparison of GFRP and CFRP ..... 52
**5 CONCLUSION AND OUTLOOK ..... 55**
**6 REFERENCES ..... 57**
**7 APPENDIX ..... 61**
7.1 GFRP ..... 61
7.2 CFRP ..... 68

# SYMBOLS

| Abbreviation | Long form |
|---|---|
| 5%/max | 5% increased compliance or maximum load |
| AE | acoustic emission |
| AST | auto sensor test |
| BT | beam theory |
| CBT | corrected beam theory |
| CBTE | corrected beam theory using effective crack length |
| CFRP | carbon fiber reinforced polymer |
| DCB | double cantilever beam |
| DIC | digital image correlation |
| ECM | experimental compliance method |
| ELS | end loaded split |
| ENF | end-notached flexural |
| FRMM | fixed ratio mixed mode |
| FRP | fiber reinforced polymer |
| GFRP | glass fiber reinforced polymer |
| HDT | hit definition time |
| HLT | hit lockout time |
| LEFM | linear elastic fracture mechanics |
| MCC | modified compliance calibration |
| MMB | mixed mode bending |
| NL | non linearity |

| | |
|---|---|
| PDT | peak definition time |
| SBT | simple beam theory |
| VIS | visual onset |

| **Designation** | **Description** | **Unit** |
|---|---|---|
| G | Energy Release Rate | $J/m^2$ |
| $G_c$ | Critical Energy Release Rate | $J/m^2$ |
| K | Stress intensity factor | $MPam^{0.5}$ |

# LIST OF FIGURES

Figure 2.1: Basic modes of crack loading: mode I (opening), mode II (in-plane shear) and mode III (out-of-plane shear) [16]. ..... 11

Figure 2.2: An infinitely wide plate containing a through-thickness crack [16]. ..... 12

Figure 2.3: Driving force and R Curve diagrams for a) flat and b) rising R curve [16]. ..... 14

Figure 2.4: AE detection system [6]. ..... 17

Figure 2.5: Analysis methods for AE signals [24]. ..... 18

Figure 2.6: Basic features of an AE signal [28]. ..... 19

Figure 3.1: DCB specimen for mode I testing a) dimensions and b) marked at regular increments. ..... 23

Figure 3.2: Specimen for mode II ELS and mixed mode I/II FRMM testing a) dimensions and b) marked at regular increments. ..... 24

Figure 3.3: Test setup for MMB. ..... 25

Figure 3.4: Configurations for a) Double Cantilever Beam (DCB), b) Ent-notched flexural (ENF), c) End-loaded split (ELS), d) Fixed ratio mixed mode (FRMM) and e) Mixed mode bending (MMB) tests [33]. ..... 26

Figure 3.5: Optical determination of critical energy release rate. ..... 28

Figure 3.6: a) Onset points according to standard methods and by AE and b) determination of crack initiation with the use of AE. ..... 29

Figure 4.1: Force-displacement curve of a GFRP DCB test according to ISO 15024 - 01 (cross-head speed = 1 mm/min). ..... 32

Figure 4.2 R-curve of a GFRP DCB test according to ISO 15024 - 01 (cross-head speed = 1 mm/min). ..... 32

Figure 4.3: Comparison of AE source localization and optically observed crack front during a GFRP DCB test according to ISO 15024 - 01 (cross-head speed = 1 mm/min). ..... 33

Figure 4.4: Force-displacement curve of a GFRP ELS test according to ISO/DIS 15114 – 12 (cross-head speed = 0,5 mm/min)..... 34

Figure 4.5: R-curve of a GFRP ELS test according to ISO/DIS 15114 - 12 (cross-head speed = 0,5 mm/min)..... 34

Figure 4.6: Comparison of AE source localization and optically observed crack front during a GFRP ELS test according to ISO/DIS 15114 - 12 (cross-head speed = 0,5 mm/min). ..... 35

Figure 4.7: Force-displacement curve of a GFRP ENF test according to ASTM D7905 – 14 (cross-head speed = 0,5 mm/min)..... 36

Figure 4.8: Force-displacement curve of a GFRP FRMM test according to ESIS TC4 Protocol (cross-head speed = 1 mm/min)..... 36

Figure 4.9: R-curve of a GFRP FRMM test according to ESIS TC4 Protocol (cross-head speed = 1 mm/min)..... 37

Figure 4.10: Comparison of AE source localization and optically observed crack front during a GFRP FRMM test according to ESIS TC4 Protocol (cross-head speed = 1 mm/min). ..... 37

Figure 4.11: Force-displacement curve of a GFRP MMB test according to ASTM D6671 - 13 (cross-head speed = 0,5 mm/min)..... 38

Figure 4.12: R-curve of a GFRP MMB test according to ASTM D6671 – 13 (cross-head speed = 0,5 mm/min)..... 38

Figure 4.13: Fracture surfaces of GFRP for a) mode I DCB, b) mode II ELS, c) mode II ENF, d) mixed mode I/II FRMM and e) mixed mode I/II MMB. ..... 40

Figure 4.14: Results for all tested modes for GFRP. ..... 42

Figure 4.15: Force-displacement curve of a CFRP DCB test according to ISO 15024 - 01 (cross-head speed = 1 mm/min)..... 43

Figure 4.16 R-curve of a CFRP DCB test according to ISO 15024 - 01 (cross-head speed = 1 mm/min)..... 43

Figure 4.17: Comparison of AE source localization and optically observed crack front during a CFRP DCB test according to ISO 15024 – 01 (cross-head speed = 1 mm/min). ..... 44

Figure 4.18: Force-displacement curve of a CFRP ELS test according to ISO/DIS 15114 – 12 (cross-head speed = 0,5 mm/min)..... 44

Figure 4.19: R-curve of a CFRP ELS test according to ISO/DIS 15114 - 12 (cross-head speed = 0,5 mm/min). ..... 45

Figure 4.20: Comparison of AE source localization and optically observed crack front during a CFRP ELS test according to ISO/DIS 15114 - 12 (cross-head speed = 0,5 mm/min)..... 45

Figure 4.21: Force-displacement curve of a CFRP ENF test according to ASTM D7905 – 14 (cross-head speed = 0,5 mm/min)..... 46

Figure 4.22: Force-displacement curve of a CFRP FRMM test according to ESIS TC4 Protocol (cross-head speed = 1 mm/min)..... 47

Figure 4.23: R-curve of a CFRP FRMM test according to ESIS TC4 Protocol (cross-head speed = 1 mm/min). ..... 47

Figure 4.24: Comparison of AE source localization and optically observed crack front during a CFRP FRMM test according to ESIS TC4 Protocol (cross-head speed = 1 mm/min). ..... 48

Figure 4.25: Force-displacement curve of a CFRP MMB test according to ASTM D6671 - 13 (cross-head speed = 0,5 mm/min)..... 48

Figure 4.26: R-curve of a CFRP MMB test according to ASTM D6671 – 13 (cross-head speed = 0,5 mm/min). ..... 49

Figure 4.27: Fracture surfaces of CFRP for a) mode I DCB, b) mode II ELS, c) mode II ENF, d) mixed mode I/II FRMM and e) mixed mode I/II MMB. ..... 50

Figure 4.28: Results for all tested modes for CFRP. ..... 52

Figure 4.29: Fiber bridging of a a) GFRP and b) a CFRP specimen during DCB testing. ..... 53

Figure 4.30: Comparison of results of GFRP and CFRP. ..... 54

Figure 7.1: a) Force-displacement curve and b)-e) R-curves of GFRP DCB tests according to ISO 15024 (cross-head speed = 1 mm/min). ..... 63

Figure 7.2: a) Force-displacement curve and b)-e) R-curves of GFRP ELS tests according to ISO/DIS 15114 - 12 (cross-head speed = 0,5 mm/min). ..... 64

Figure 7.3: Force-displacement curve of GFRP DCB tests according to ASTM D7905 -14 (cross-head speed = 0,5 mm/min)..... 65

Figure 7.4: a) Force-displacement curve and b)-e) R-curves of GFRP FRMM tests according to ESIS TC4 Protocol (cross-head speed = 1 mm/min). ..... 66

Figure 7.5: a) Force-displacement curve and b)-e) R-curves of GFRP MMB tests according to ASTM D6671-13 (cross-head speed = 0,5 mm/min). ..... 67

Figure 7.6: a) Force-displacement curve and b)-e) R-curves of CFRP DCB tests according to ISO 15024 (cross-head speed = 1 mm/min). ..... 70

Figure 7.7: a) Force-displacement curve and b)-e) R-curves of CFRP ELS tests according to ISO/DIS 15114 - 12 (cross-head speed = 0,5 mm/min). ..... 71

Figure 7.8: Force-displacement curve of CFRP DCB tests according to ASTM D7905 -14 (cross-head speed = 0,5 mm/min)..... 72

Figure 7.9: a) Force-displacement curve and b)-e) R-curves of CFRP FRMM tests according to ESIS TC4 Protocol (cross-head speed = 1 mm/min). ..... 73

Figure 7.10: a) Force-displacement curve and b)-e) R-curves of CFRP MMB tests according to ASTM D6671-13 (cross-head speed = 0,5 mm/min). ..... 74

# LIST OF TABLES

Table 1: Standard test methods for quasi-static delamination tests of FRP laminates. ..... 16

Table 2: A selection of features and their description [24]. ..... 20

Table 3: Overview of standard test methods with test speed and specimen dimensions. 25

Table 4: Energy release rates of a GFRP ENF test according to ASTM D7905 – 14 (cross-head speed = 0,5 mm/min). ..... 35

Table 5: Energy release rates of a CFRP ENF test according to ASTM D7905 – 14 cross-head speed= 0,5 mm/min. ..... 46

Table 6: Overview of all GFRP results, obtained from average values of all calculation methods according to each norm. ..... 61

Table 7: Initiation results of GFRP ENF tests according to ASTM D7905 - 14 (cross-head speed = 0,5mm/min). ..... 65

Table 8: Overview of all CFRP results, obtained from average values of all calculation methods according to each norm. ..... 68

Table 9: Initiation results of CFRP ENF tests according to ASTM D7905 - 14 (cross-head speed = 0,5mm/min). ..... 72

# 1 INTRODUCTION

Fiber reinforced materials can be found in a variety of applications. The principle of absorbing forces by fibers has always been utilized by nature to yield the best lightweight structures. In addition, fiber reinforced materials have the advantage of combining more than one material, and therefore the opportunity to compensate shortcomings of individual materials. Composite materials are characterized by their high toughness and stiffness while having a low density. Those characteristics make composites a perfect material for lightweight applications [1–3].

However, in composite materials it is not unusual to find inhomogeneities or defects from manufacturing or the handling of components. These defects can initiate cracks, that can propagate through the material and lead to the failure of the component. To analyze and characterize the delamination behavior of composites, fracture mechanical parameters, such as the critical energy release rate, can be determined. In order to do so, crack initiation and propagation have to be detected.

It is still state of the art to measure crack propagation optically using a microscope or camera system to rewatch the crack growth after the test. This measurement technique leads to subjective and imprecise results as well as few data points. In the master's thesis of Jutta Geier, two methods to automate crack detection have been proposed, Digital Image Correlation and Infrared Thermography [4]. Another method that could be used is acoustic emission (AE). AE is a non-destructive test method, which uses transient stress waves generated by crack growth or other material degradation processes [5,6]. The stress waves travel through the material and are detected by piezoelectric sensors at the specimen's surface. When using at least two sensors, the origin of the detected signals can be calculated based on the difference of arrival time. Therefore, AE states a promising technique to localize the propagation of the crack front during delamination resistance testing of FRP laminates.

Furthermore, AE can be used for the determination of delamination initiation, as it is a highly sensitive test method. The standard methods typically employed can yield results that vary significantly and are highly subjective. This was shown in a round robin test, where

36 researchers had to interpret the point of non-linearity on the same load-displacement curve from a mode I test conducted on a unidirectional carbon fiber reinforced polymer composite. The results scattered around 5 % [7].

The scope of this thesis was to characterize the fracture mechanical behavior of glass (GFRP) and carbon fiber reinforced laminates (CFRP) with the same epoxy matrix system to determine mode I, II and mixed mode I/II interlaminar fracture toughness. Furthermore, a special focus was given to the method of AE as an additional tool to monitor delamination behavior. Since AE is a highly sensitive method it can be used to detect occurring damage events on a microscopic level before any macroscopic damage is visible. Therefore, AE was used to evaluate the point of crack initiation and compare it to the results obtained by the methods according to the test standards. Moreover, AE signals were localized, and crack growth observed with AE was compared to the optically detected delamination behavior.

# 2 THEORETICAL BACKGROUND

## 2.1 Delamination of composites

Fiber reinforced polymers (FRP) consist of at least two materials, containing a fiber and matrix material. The used materials differ in their properties, as a consequence tailored properties of the composite can be achieved. FRPs find application in large-scale components such as boats, wind turbine blades, airplane components but also in smaller components in the vehicle or electro industry or in sports equipment, for example ski or tennis rackets [8].

Since fiber reinforced materials consist of more than one material, failure mechanisms can occur in either one of the materials or in more than one. As common failure mechanisms of fiber reinforced polymers matrix cracking, fiber breakage and fiber-matrix debonding can be named. Matrix cracking describes a failure mechanism which occurs when the matrix strain reaches its maximum [9]. Fiber breakage describes failure when the fiber strain reaches its maximum under tensile stress. This form of failure is considered less as breakage of filaments, but as an almost simultaneous failure of fiber bundles consisting of hundreds of individual fibers in a width of at least a few millimeters. Since fiber breakage occurs at very high loads, it is considered as a non-tolerable failure mechanism. The separation of fiber and matrix is called fiber-matrix debonding. Delamination combines fiber-matrix debonding and matrix cracking and depicts the separation of two layers of the FRP material caused by interlaminar stress between the layers [1,9]. A factor that influences delamination behavior of composites is fiber bridging. This phenomenon describes fibers of adjacent plies that bridge over the delamination plane and serve as crack arrestors, which leads to an increasing delamination resistance and interlaminar fracture toughness. Although fiber bridging is considered as a favorable phenomenon, it makes it more challenging to characterize the onset and growth of delamination [10].

Delamination of FRP materials is considered a critical failure mechanism because delamination can reduce the stiffness of the structure and therefore weaken the whole component and reduce its lifetime [11]. As a consequence, it is important to gain a deep

insight into the delamination behavior of FRPs. In order to describe the conditions for delamination growth the concept of fracture mechanics is used.

Fracture mechanics assumes, that each body or structure contains cracks of various sizes, either due to a non-perfect production technique or introduced by external stresses during usage. As a consequence, failure of a component and its material occurs due to the propagation of cracks. Fracture mechanics analyses the condition for crack propagation and establishes quantitative relationships between external load, nominal stress, applied on a component or test specimen, the size and shape of the cracks, and the material's resistance to crack propagation [12].

Crack growth can occur in different modes: Mode I, II and III, depending on the direction of the applied load and therefore the different movement of the crack surfaces, as shown in Figure 2.1.There is mode I (crack opening, tensile mode), where the load is applied perpendicular to the crack surfaces, which are moved directly apart, mode II (in-plane shearing mode), where the crack surfaces are moved over each other perpendicular to the crack front and mode III (out-of-plane shearing mode), where the crack surfaces are moved over each other parallel to the propagated crack. Furthermore mixed mode, a combination of more than one mode can be named [13,14]. A crack always propagates into the direction of the least resistance, therefore it often does not stay in its initial plane. A crack trying to change direction of planes in order to get into a mode I configuration is called mode I branch [15]. Since this often occurs for mode III, this thesis will only concentrate on mode I, II and mixed mode I/II.

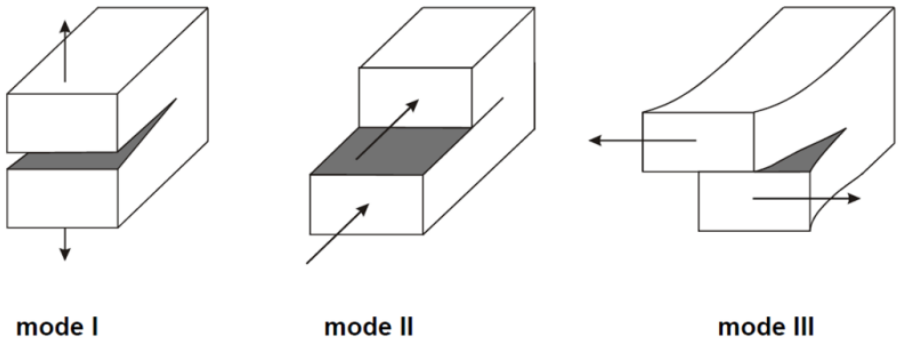


Figure 2.1: Basic modes of crack loading: mode I (opening), mode II (in-plane shear) and mode III (out-of-plane shear) [16].

Standardized test methods for delamination resistance testing of composites are based on linear elastic fracture mechanics. In the following section an overview of this concept and the relevant fracture mechanical parameters will be given.

### 2.1.1 Linear Elastic Fracture Mechanics

Linear Elastic Fracture Mechanics (LEFM) assumes that all dissipated energy is related to the fracture process, material behavior is linear elastic and the crack tip is perfectly sharp. Based on that, LEFM describes the energy change during the increase of the crack area. When testing metals and polymers, typically plasticity and non-linear effects take place. However, if this non-linearity is comparatively small, the approach of LEFM can be applied. It simplifies the analysis and makes the development of effective testing methods possible [17].

In 1921, Griffith assumed that when a plate made of an elastic material with applied stress contains a crack, a decrease in potential energy and an increase in surface energy can be observed as the crack propagates. The decrease of potential energy is due to the release of stored energy and the work performed by external loads. With an increasing crack length new surface area is created, leading to a non-equilibrium state of atoms at the surface and thus requiring the expenditure of surface energy [18]. Figure 2.2 shows an infinite plate with a crack of length 2a and a uniform tensile stress, σ.

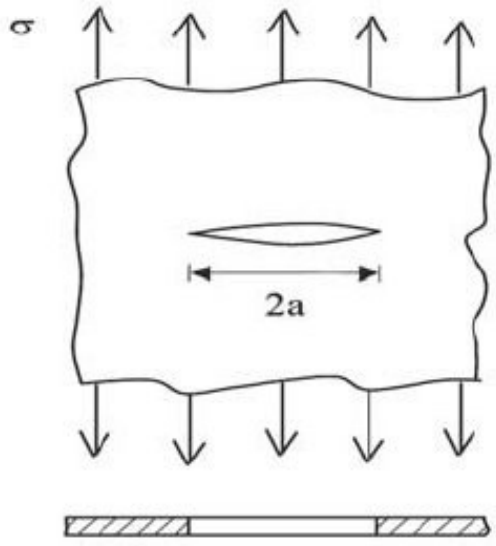


Figure 2.2: An infinitely wide plate containing a through-thickness crack [16].

The total energy, U, of the cracked plate can be expressed as

$$U = U_0 + U_a + U_\gamma \tag{2.1}$$

$U_0$ = elastic energy of the uncracked plate

$U_a$ = elastic energy caused by the introduction of a crack in the plate

$U_\gamma$= elastic surface energy caused by the formation of the crack surface

Equation 2.2 and 2.3, where E is the elastic modulus and ν is the poisson's ratio, show the energy release rate, G, which states the elastic energy available per unit crack surface area for infinitesimal crack extension, for either plane stress or plane strain [19].

Plane stress $$\frac{dU_a}{da} = G = \frac{\pi\sigma^2 a}{E} \tag{2.2}$$

Plane strain $$\frac{dU_a}{da} = G = (1 - \vartheta^2)\frac{\pi\sigma^2 a}{E} \tag{2.3}$$

To determine the materials fracture toughness another approach can be applied by describing the local stress field around the crack tip. Due to the assumption of a perfectly sharp crack, there is a stress singularity at the crack tip. Therefore, within a certain region in front of the crack tip the yield stress is reached, leading to the formation of a plastic zone. As long as the plastic zone is relatively small compared to the specimen, LEFM can still be applied. Cracks can show different magnitudes of the stress field parameter, which is defined as the stress intensity factor, K [19,20]. K stands for the driving force for crack propagation, and its critical value, $K_C$, is the fracture toughness, which characterizes the material's resistance to crack extension [18]. K can be calculated as shown in equation 2.4, where f(a/w) is a dimensionless parameter which depends on the geometry of the specimen and crack [19].

$$K = \sigma\sqrt{\pi a}\, f\left(\frac{a}{w}\right) \tag{2.4}$$

The relation of $K_C$ and $G_C$ for plane stress and plane strain are shown in equation 2.5 and 2.6 [12,18,19].

For plane stress $$G_C = \frac{K_{IC}^2}{E} \tag{2.5}$$

For plane strain $$G_C = \frac{K_{IC}^2}{E} * (1 - \vartheta^2) \tag{2.6}$$

The crack resistance curve, also called R curve, demonstrates if crack growth occurs either stable or unstable. Figure 2.3 shows examples for crack resistance, and the corresponding G versus crack size curves, also called driving force curves. Figure 2.3a shows a flat R curve due to the material's constant resistance with crack growth. As long as the stress is at $\sigma_1$, the crack growth occurs stable. When the stress reaches $\sigma_2$, the crack propagation happens unstable, and fracture occurs due to the increasing driving force with crack growth and a constant resistance curve. On the other side, Figure 2.3b shows a rising R curve. The crack grows a bit as soon as the stress reaches $\sigma_2$ but can only grow further if the stress increases. As long as the stress remains at the same level, the driving force increases slower than the resistance, therefore no crack propagation occurs. Crack growth is still stable when the stress reaches $\sigma_3$. When the stress increases to $\sigma_4$, the driving force curve is tangent to the R curve. After that point, unstable crack growth occurs, due to a higher change in driving force compared to the slope of the R curve [16].

For materials with a flat R curve a critical energy release rate, $G_c$, can be defined without any difficulties. For materials with a rising R curve, $G_c$ must not be defined at a single value. According to Figure 2.3b, the critical value occurs when the driving force curve intersects the R curve tangentially. However, this point is influenced by the shape of the driving force curve, which depends on the structure's configuration. For example, looking at the configuration as it can be seen in Figure 2.2, the driving force curve would be linear, but for a double cantilever beam (DCB) specimen configuration G varies with $a^2$ [16].

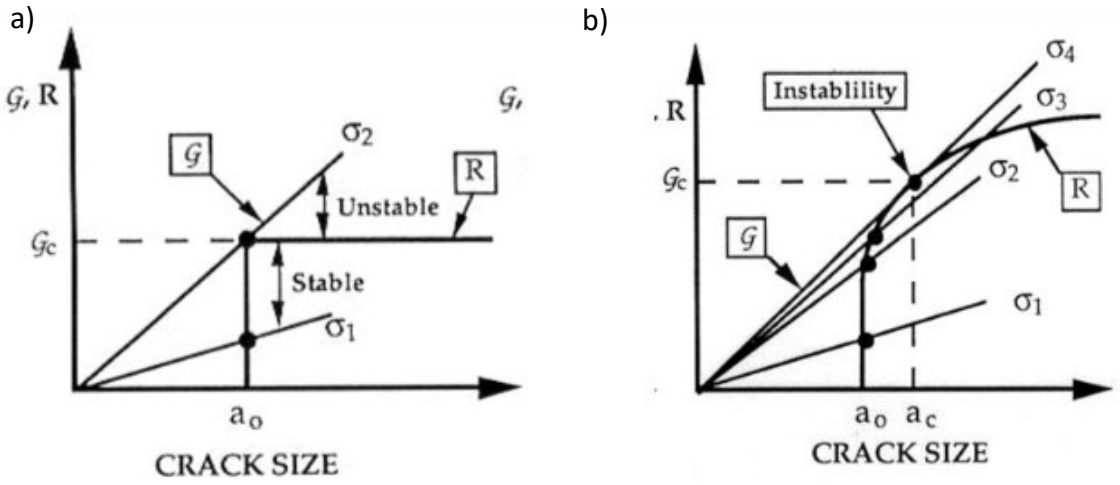


Figure 2.3: Driving force and R Curve diagrams for a) flat and b) rising R curve [16].

Consequently, the critical energy release rate values at a given R curve would vary for these different configurations. Hence, for materials with a rising R curve, the energy release rate at the onset of crack initiation can be used as a characterization parameter. The initiation value usually does not depend on the structure of the configuration, but it is challenging to define the precise moment of crack initiation. Different concepts have been developed, which will be explained in the next chapter [16].

### 2.1.2 Norms / Standards

The application of fracture mechanics to fiber reinforced composites can lead to difficulties since conventional fracture mechanics assumes that a single crack grows and increases in size while its shape and orientation remains constant. Looking at fiber reinforced polymers, fracture is often associated with microcracks throughout the material. But there are situations where it is appropriate to apply fracture mechanics on composite materials. For instance, for interlaminar fracture in fiber reinforced materials LEFM is applicable. A delamination front can be handled as a crack and the material's resistance to the propagation of this crack can be called fracture toughness. To measure the interlaminar fracture toughness several different standardized test methods have been published [16]. Since the fracture toughness depends on the applied mode, which has been shown earlier, different standardized test methods had to be established. Table 1 provides an overview of standards that are available for quasi-static delamination tests conducted on continuous fiber reinforced materials.

For each mode different standard test methods are available, the different configurations are explained more in detail later and therefore shown in Figure 3.4. For mode I testing the double cantilever beam (DCB) method is used. Schuecker and Davidson showed that end-notched flexural Test (ENF) and four-point bend end-notched flexure (4ENF) can yield in similar values for fracture toughness for mode II [21]. Brunner states that 4ENF shows stable crack propagation while ENF does not. Another mode II method is the end-loaded split test (ELS) which shows stable crack growth as well. For mixed mode I/II two promising methods exist, mixed mode I/II bending (MMB), for which the ratio of mode I to mode II can be adjusted, and fixed ratio mixed mode I/II testing (FRMM), which is limited to a ratio

4:3 [22]. In this thesis, one test method for mode I and two different standard test methods for both mode II and mixed mode I/II should be compared to each other.

Table 1: Standard test methods for quasi-static delamination tests of FRP laminates.

| Mode | Standard test method | Standard test in preparation |
|---|---|---|
| I | JIS K 7086<br>ASTM D 5528<br>ISO 15024<br>HB 7402<br>AITM 1-0005<br>BSS 7273<br>EN 6033 | |
| II | JIS K 7086<br>AITM 1-0006<br>ASTM D7905<br>ISO 15114<br>EN 6034 | ASTM WK 22949 |
| I/II | ASTM D6671 | ESIS TC4 Protocol [23] |

## 2.2 Acoustic Emission

Acoustic Emission (AE) is defined as spontaneously released transient elastic energy during deformation or fracture of materials. The analysis of these signals is considered as a nondestructive testing method, which uses the transient stress waves generated by crack growth or other material degradation processes [5]. Compared to other nondestructive testing methods, its advantage is that the crack front in the specimen can be observed during the entire loading process without influencing the specimen and the results [6].

AE signals occur from microscopic displacements in a solid body. For fiber reinforced materials, the most common source of AE signals is the initiation and growth of cracks. On a microscopic scale, these can be described as the generation and propagation of cracks inside the matrix, in the interface between matrix and fiber or between fibers. Friction of crack surfaces, especially during unloading and reloading can be named as another signal source [24]. This chapter should give an overview of the principle, the signal analysis and detection, source localization as well as applications of AE.

### 2.2.1 Principle

In Figure 2.4 a configuration of an AE detection system is shown. Acoustic waves are detected by the AE sensor, which transforms the surface's dynamic motions into electrical signals. Since those signals are normally weak, a pre-amplifier and a main-amplifier are used to amplify them. Furthermore, a band-pass filter is used to eliminate any noise [6].

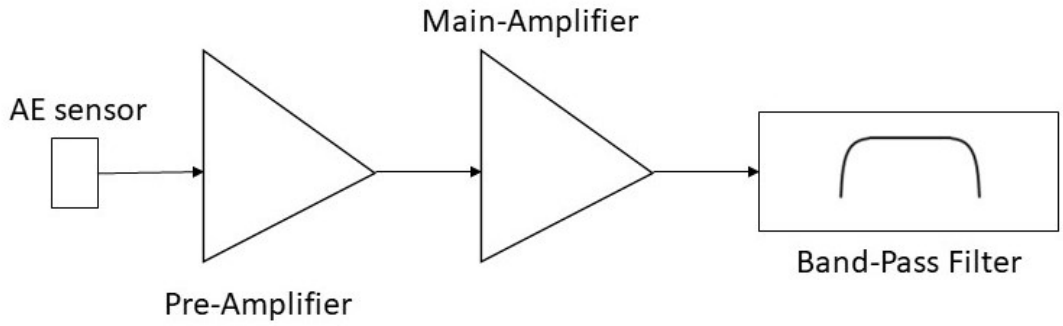


Figure 2.4: AE detection system [6].

AE analysis requires a resonant or broadband sensor, a preamplifier, and an acoustic emission analyzer to be performed [14]. Depending on the source of the signal, the signals form can be different. Frequencies of signals from composite materials are often in a range of 50 to 600 kHz [25,26]. Most AE systems are provided with a bandwidth of 100 kHz to 2 MHz [27].

The surface of a solid material is where AE signals are detected. Mostly piezoelectric materials are used to detect wave amplitudes down to the order of $10^{-13}$ to $10^{-14}$m [24]. Piezoelectric transducers are most commonly used [28]. As a sensor, the piezoelectric element is covered in a housing and attached to the solid surface by a viscous coupling medium. The sensor's primary purpose is to convert the solid's surface motion into an electric signal. This conversion is based on the piezoelectric effect [24].

When fracture occurs, it generates an AE signal. As soon as that signal surpasses the threshold and causes a system channel to collect data it is classified as a hit [6]. Once an AE hit is detected, it has to be assessed. Therefore, three parameters, illustrated in Figure 2.6, have been established: the hit definition time (HDT), the hit lockout time (HLT) and the peak definition time (PDT). HDT defines the maximum time frame between threshold

crossings. If no crossing happens during this time frame, the hit ends. If HDT is set too high, several hits are classified as one. If set too low, the system cannot detain the whole hit, and may consider one hit as several individual hits instead. HLT defines the duration that should be between two captured hits. If HLT is set too high, the system may not be able to capture the next signal and if set too low, parts close to the end of the hit may not be captured. PDT establishes the timeframe within which the peak value has to be determined after the detection of a hit. If set too high the chances of getting wrong peak values increase. The PDT should be set as low as possible, but if too low, the true peak value may not be determined correctly [28].

### 2.2.2 Analysis of Acoustic Emission signals

Figure 2.5 shows possible techniques to analyze AE signals. The AE activity can be determined by counting the detected signal. Furthermore, the AE source position can be localized, and the detected signals can be categorized into classes. If this procedure is performed successfully, the amount of damage, the position of damage and the type of damage can be determined. The combination of these three methods can give valuable information about the failure of fiber reinforced composites [24].

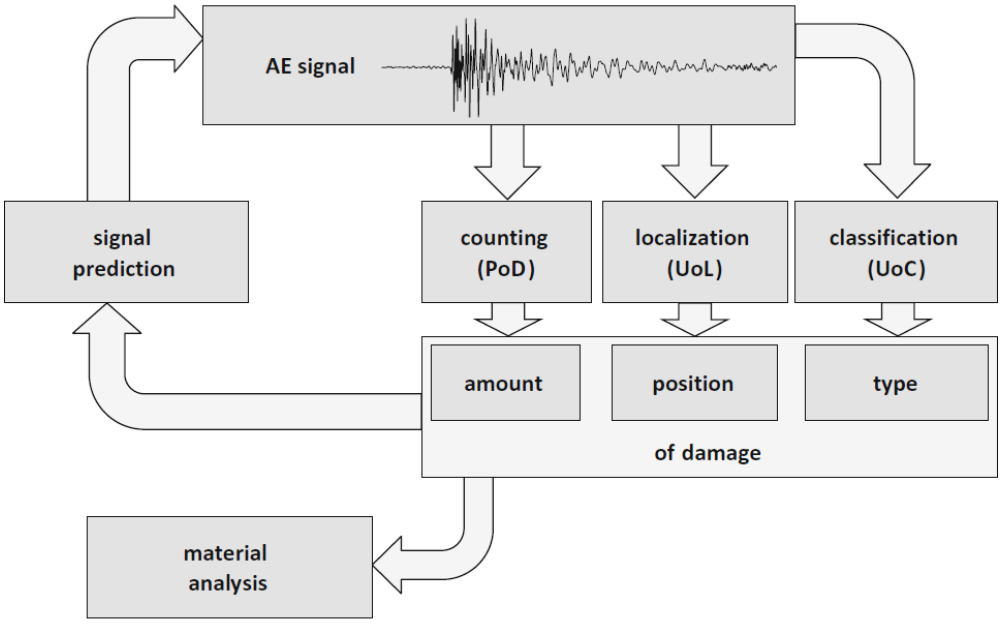


Figure 2.5: Analysis methods for AE signals [24].

Counting the signals is a standard technique, but it goes with an uncertainty, given by the probability of detection (PoD). Even though the localization of source position is well established, it is more difficult when the specimen is made of an anisotropic and inhomogeneous material such as fiber reinforced polymers. Source localization under laboratory conditions using test specimens can yield valuable results, but applying localization techniques in realistic structures, such as multi-material combinations or hybrid joints can be challenging. As a consequence, source localization is associated with an uncertainty of localization (UoL). There is a wide range of methods available for grouping AE signals, from basic approaches such as discrete feature values to more advanced techniques with automated or semi-automated pattern recognition techniques. But again, every result is subject to uncertainty of classification (UoC). When the signals have been successfully grouped, specific source mechanisms must be assigned. Usually, this task is accomplished by phenomenological observations, comparative measurements of test specimens with known AE sources, or microscopy [24].

Once an AE hit is determined, for each AE signal basic features can be obtained. Figure 2.6 and Table 2 show AE basic features and their descriptions.

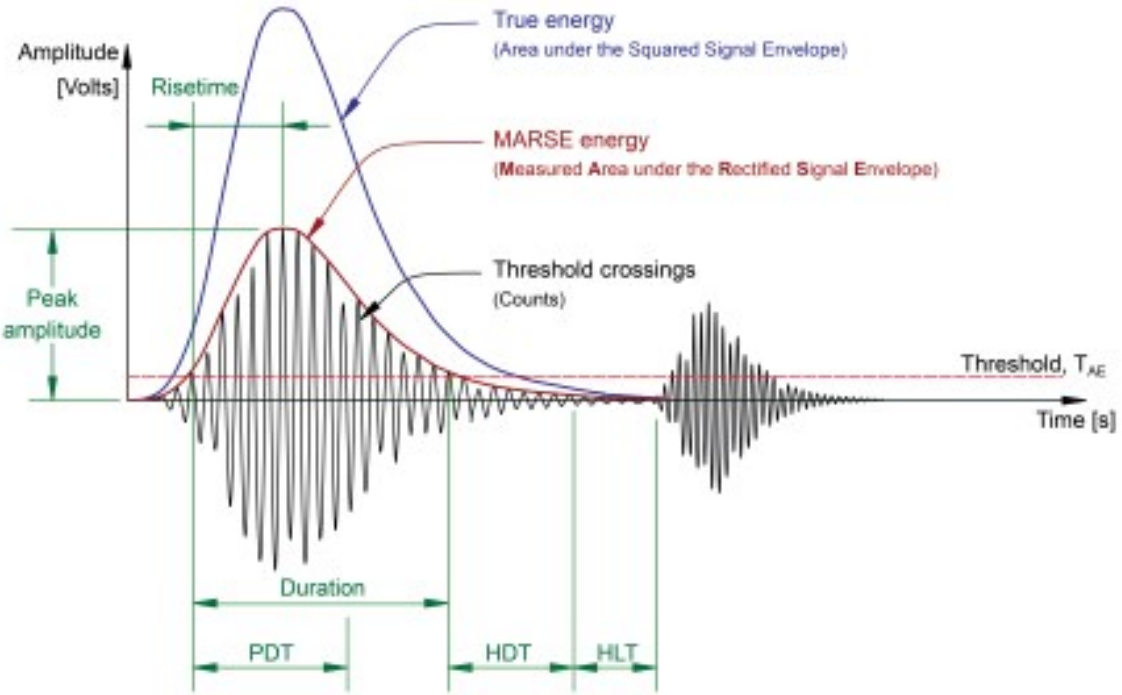


Figure 2.6: Basic features of an AE signal [28].

Table 2: A selection of features and their description [24].

| **Feature** | **Unit** | **Description** |
|---|---|---|
| Duration | [µs] | Time between first and last threshold crossing |
| Amplitude | [dB] | $dB_{AE} = 20 \log\left(\frac{U_{max}}{1\mu V}\right) - dB_{preamplifier}$ |
| Counts | [1] | Number of threshold crossings |
| Rise time | [µs] | Time between first threshold crossing and time of maximum signal voltage |
| Counts to peak | [1] | Number of threshold crossings during rise time |
| Absolute energy | [J] | Integral of the energy squared |
| Peak frequency | [Hz] | Frequency of peak signal contribution |
| Frequency centroid | [Hz] | X component of centroid of the FFT spectrum |
| Weighted peak frequency | [Hz] | Geometric mean of the peak frequency and the frequency centroid |
| Partial power | [%] | The area integral between two limits of a Fast Fourier Transform (FFT) spectrum with respect to the total area |

### 2.2.3 Source Localization

Algorithms for source localization use the differences of the arrival time between several sensor positions in order to localize a signal's origin. Therefore, the arrival time needs to be determined correctly. The simplest approach is to define the first time a signal is passing a selected threshold as its onset. However, this can be a challenge because depending on the chosen threshold level, the arrival time can be incorrect [24].

When the arrival time is determined, the source localization can be carried out by the zonal localization. The sensor that shows the arrival of the wave first is the closest to the source position. The area of that sensor is called source "zone". Nevertheless, the accuracy of the determination of the source position is limited to a precision of roughly around half the

sensor spacing. Based on the arrival times of the sensors the source position $r_0$ and time of signal emission $t_0$ can be calculated, as shown in equation 2.15, which correlates the position of the sensor $r_i$ and the signal arrival time $t_i$ with the source location $r_0$ and sound velocity c. As soon as an AE source has successfully been localized, it is called an AE event [24].

$$|r_i - r_0| = c \cdot (t_i - t_0) \tag{2.15}$$

Elastic waves can either be longitudinal or transversal bulk waves. In transversal waves particles move perpendicular to the direction of propagation of the disturbance. In longitudinal waves on the contrary, particles move in the direction of propagation due to tension and compression forces [29]. Those waves also differ in different wave velocities, which can be calculated with equation 2.16 and 2.17 [24]. Since the wave velocities depend on the elastic modulus E and the poisson's ratio ν, they are direction dependent in composite materials due to their anisotropic nature.

$$c_{longitudinal} = \sqrt{\frac{E(1-\nu)}{\rho(1+\vartheta)(1-2\nu)}} \tag{2.16}$$

$$c_{transversal} = \sqrt{\frac{E}{2\rho(1+\nu)}} \tag{2.17}$$

In thin plates, like composite laminates, structured guided waves can be found. These so-called Lamb-type guided waves, have frequency dependent propagation velocities and reduce a 3D localization problem to a 2D localization problem since it is not possible to localize the depth position of the AE source. Besides composites' anisotropic properties and frequency dependent propagation velocities, attenuation or material degradation can affect source localization and need to be considered [24].

### 2.2.4 Application to Delamination Resistance Testing of FRP Laminates

Due to the fact that AE enables the detection of a multitude of microscopic failure mechanisms in composites, there is a wide range of applications for AE. The following should state some of the most used applications of AE analysis in delamination resistance testing of FRP laminates.

Using AE signals enables the determination of the first failure onsets in the context of fracture mechanics. The onset of damage in a certain material correlates with the onset of the AE signal. This approach is only allowed if there is no background noise. Even if ideal laboratory conditions are employed, the detection of the first acoustic signal and the detection of first damage onset are not equal. Besides the onset of damage, AE gives the opportunity to detect the onset of specific failure modes such as inter-fiber failure and fiber failure using Puck's failure criterion. After the onsets have been evaluated, the damage evolution can be visualized by AE signals as well [24]. Brunner showed in a previous paper source localization for a mode I DCB specimen with the means of AE. The paper concludes that in the process zone around the delamination tip signal sources with high amplitudes can be found [30]. Another paper from Brunner states that a correlation between the amplitude of the AE signals and the crack area can be obtained, which is an indication that matrix cracks results in delamination propagation [31]. Since the signal localization has only been made for mode I testing, this thesis will state results for mode I, mode II and mixed mode I/II source localization.

As proposed by Sause et al., another application of AE is the classification of AE signals depending on the failure mechanisms. In his work, detected signals were recorded during mode I testing and pattern recognition techniques were applied. In this approach the recorded signals were compared with those from validated simulations of different failure mechanisms, like fiber breakage, matrix cracking and interface failure. The study demonstrated that AE is applicable for the quantification of failure mechanisms in carbon and glass fiber reinforced composite materials under mode I loading conditions [32].

# 3 EXPERIMENTAL

In the following the used materials, specimen preparation and the testing procedure are explained.

## 3.1 Materials and Specimens

All of the test specimens were unidirectionally reinforced glass or carbon fiber prepreg laminates with an epoxy matrix M79 (Hexcel, Austria) as matrix material and a fiber volume fraction of about 60 %. For crack initiation, each specimen had a Teflon foil placed at the mid-thickness. Depending on the tested mode different specimen preparation according to norm was necessary.

Specimens for mode I testing were prepared according to ISO 15024-01. Therefore, two loading blocks had to be mounted, as shown in Figure 3.1a. To evaluate the crack propagation during testing, a thin coat of typewriter correction fluid was applied to the edges of the specimen. Additionally, the sample was marked with straight vertical lines at regular increments of 5 mm and with points for each millimeter in between, as shown in Figure 3.1b.

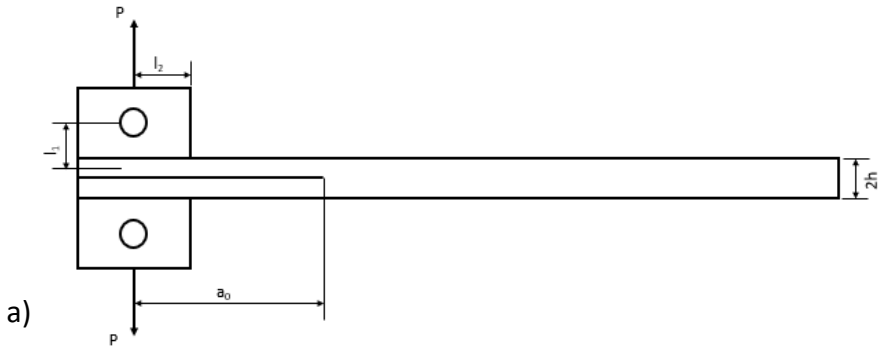


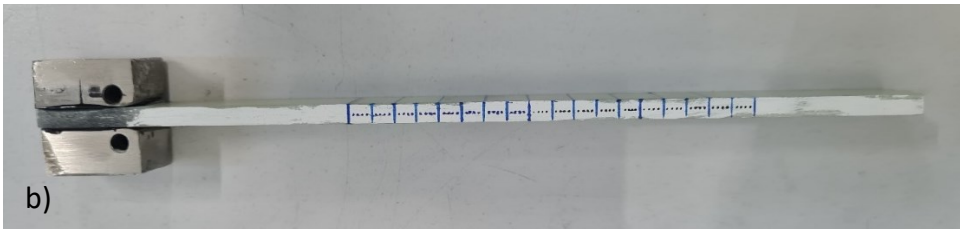


Figure 3.1: DCB specimen for mode I testing a) dimensions and b) marked at regular increments.

Mode II ELS testing was carried out according to ISO/DIS 15114-12 and FRMM according to the ESIS TC4 protocol [23]. For both methods one loading block was applied to the side of the specimen with the inserted teflon foil as shown in Figure 3.2a. To prepare the specimen for the visual measurement of crack length, a thin layer of typewriter correction fluid had to be applied to these specimens as well. Thin vertical lines had to be drawn at regular increments of 2,5 mm as illustrated in Figure 3.2b**.** According to the norm a clamp calibration has to be carried out. For the calibration the loading block was applied to the side of the specimen without the Teflon foil and marks were drawn between 50 and 110 mm from the load-block hole at 10 mm increments at one specimen per material.

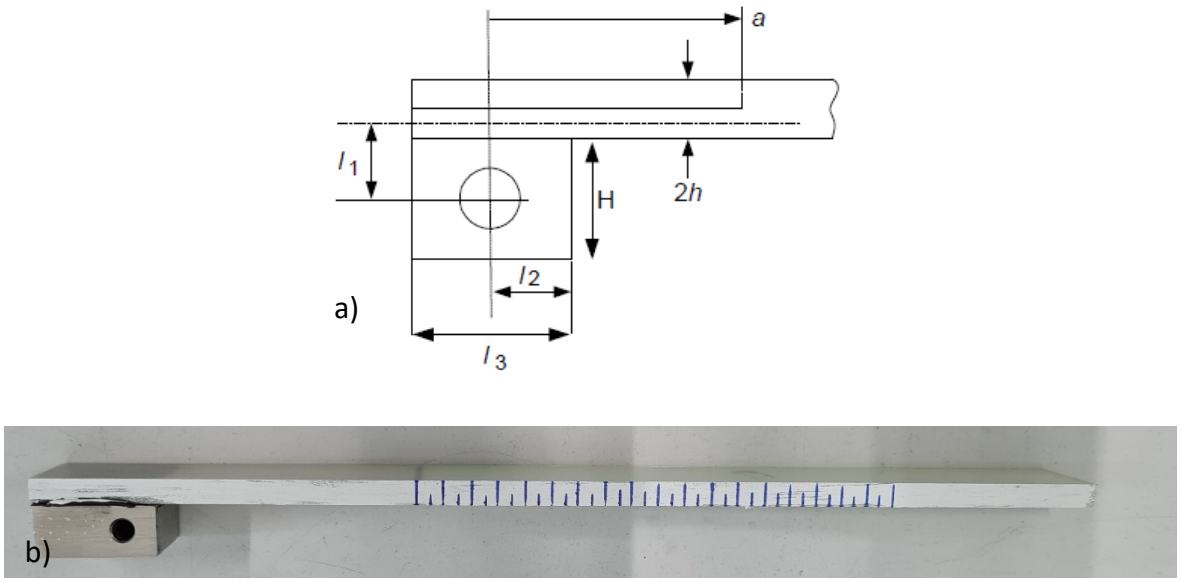


Figure 3.2: Specimen for mode II ELS and mixed mode I/II FRMM testing a) dimensions and b) marked at regular increments.

For Mode II End-Notched-Flexural (ENF) testing according to ASTM D7905-14, no loading blocks had to be attached, only marks were placed at a distance of 20, 30 and 40 mm from the tip of the insert.

According to ASTM D6671-13, another setup for mixed mode I/II was carried out, called mixed mode bending (MMB). As for the DCB setup, two loading blocks were placed, as shown in Figure 3.1. In contrast to the DCB testing, MMB testing is characterized by a combination of pull apart and bending as shown in Figure 3.3.

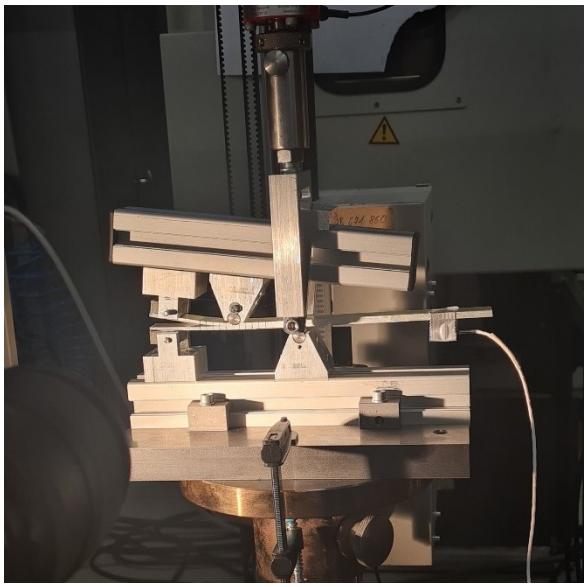

Figure 3.3: Test setup for MMB.

## 3.2 Setup

Table 3 gives an overview of the applied standard test methods, the selected test speed and specimen dimensions. The test methods were chosen to cover various different mode I, mode II and mixed mode I/II scenarios.

Table 3: Overview of standard test methods with test speed and specimen dimensions.

| **Mode** | **Test setup** | **Standard** | **Test speed [mm/s]** | **Width [mm]** | **Length [mm]** | **Insert length [mm]** |
|---|---|---|---|---|---|---|
| **I** | DCB | ISO 15024-01 | 1 | 20 | 200 | 70 |
| **II** | C-ELS | ISO/DIS 15114-12 | 0,5 | 20 | 200 | 70 |
| **II** | ENF | ASTM D7905-14 | 0,5 | 20 | 300 | 70 |
| **I/II** | FRMM | ESIS TC4 Protocol | 1 | 20 | 200 | 70 |
| **I/II** | MMB | ASTM D671-13 | 0,5 | 20 | 260 | 40 |

As mentioned above, different standard test methods were performed. Those methods differ in the test configuration, which are shown in Figure 3.4, and the calculation methods

for the energy release rate. However, most methods have very similar testing procedure, which will be explained in the following.

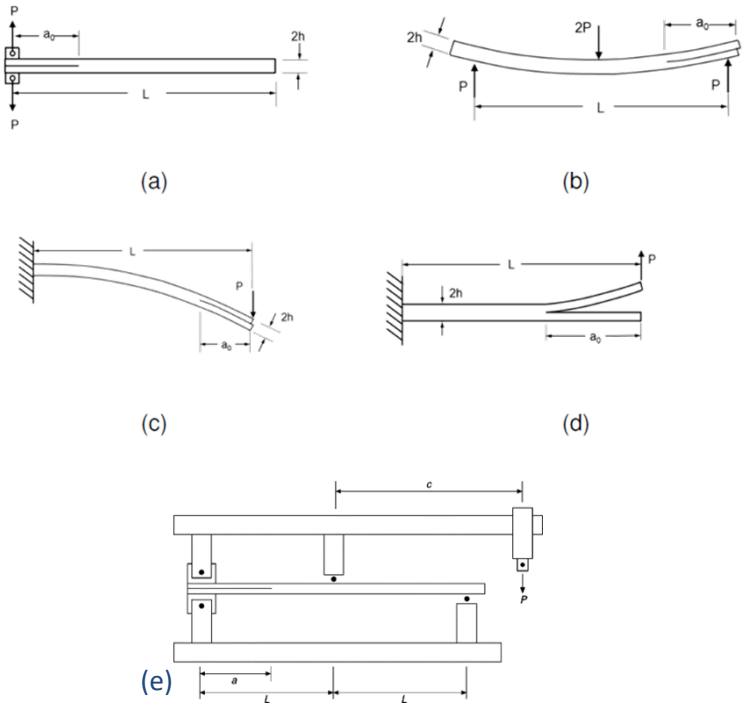


Figure 3.4: Configurations for a) Double Cantilever Beam (DCB), b) Ent-notched flexural (ENF), c) End-loaded split (ELS), d) Fixed ratio mixed mode (FRMM) and e) Mixed mode bending (MMB) tests [33].

All experimental setups were applied to a standard testing machine of the type Zwick Roell Z250 (Zwick Roell, Germany). The testing machine operates in a displacement control mode with a constant displacement rate. The load versus opening displacement is recorded continuously. To detect the crack length optically, a camera of the type Prosilica GT (Allied Vision, Germany) is positioned on one side to observe the delamination front grow along the edge during the whole test and is connected to the software MercuryRT (Mercury DIC, Czech Republic). In order to calculate the energy release rate, G, crack lengths and the respective force and displacement values are used in different approaches according to each norm. These values can be recorded and determined by the software Mercury.

The used AE system is by MISTRAS Group Inc. (Princeton Junction, USA). Two WD-sensors were attached to the specimen using silicone free vacuum grease as coupling medium. The sensors were connected to 2/4/6 preamplifiers with an amplification of 40 dB and an analogue bandpass of 20 kHz to 3 MHz The threshold was set to 35 $dB_{AE}$ and signals were recorded with a sampling rate of 5 MSPS. The PDT was set to 10 µs, HDT to 80 µs and HLT

to 300 µs. The software nAExtor by BCMtec GmbH (Augsburg, Germany) was used for source localization and feature extraction.

## 3.3 Procedure

The procedure always started with initial loading. Therefore, the specimen was loaded until the crack initiated from the foil, which was seen in a sudden drop of the load. After that the specimen was unloaded. The following step was reloading. That time the loading was not stopped at the first drop of the force, but continued until the crack has grown wide enough. This procedure was the same for all used standard methods, except for the ENF configuration. Since this setup leads to unstable crack propagation, only one data point per specimen could be obtained. Therefore, the reloading was stopped as soon as the crack propagates.

### 3.3.1 Acoustic Emission

In order to perform AE source localization, the material's speed of sound had to be measured first. Therefore, two sensors were attached to the specimen at a known distance. With the help of an Auto Sensor Test (AST) measurement the travel time between these two sensors could then be determined. By using the measured time and the known distance between the sensors the speed of sound could be calculated.

The AST feature allows a sensor to be a pulser and a receiver at the same time. Consequently, it can send out AE waves, but can also detect waves that have been sent from another sensor. Therefore the arrival time difference between two sensors can be determined [34].

During testing, one sensor was placed on one of the loading blocks and the second sensor was placed in a known distance on the specimen. For ENF testing both sensors were placed on the specimen in a known distance, since there are no loading blocks. For MMB testing only one sensor could be applied due to lack of space. Before starting the testing procedure, a pencil lead test was carried out. Therefore, a pencil lead was broken in regular increments in order to ensure a proper localization of the signals. The test procedure will be explained more into detail in the next part.

### 3.3.2 Optical evaluation

For the calculation of the critical energy release rates an optical evaluation is necessary. Therefore, as shown in Figure 3.5, the crack length, a, has to be determined for each increment with the help of the pictures taken during testing. For each specific crack length, the according load and displacement values have to be determined. These three values are necessary to calculate the energy release rate for each crack length and result in the resistance curve, which shows the energy release rate over crack length.

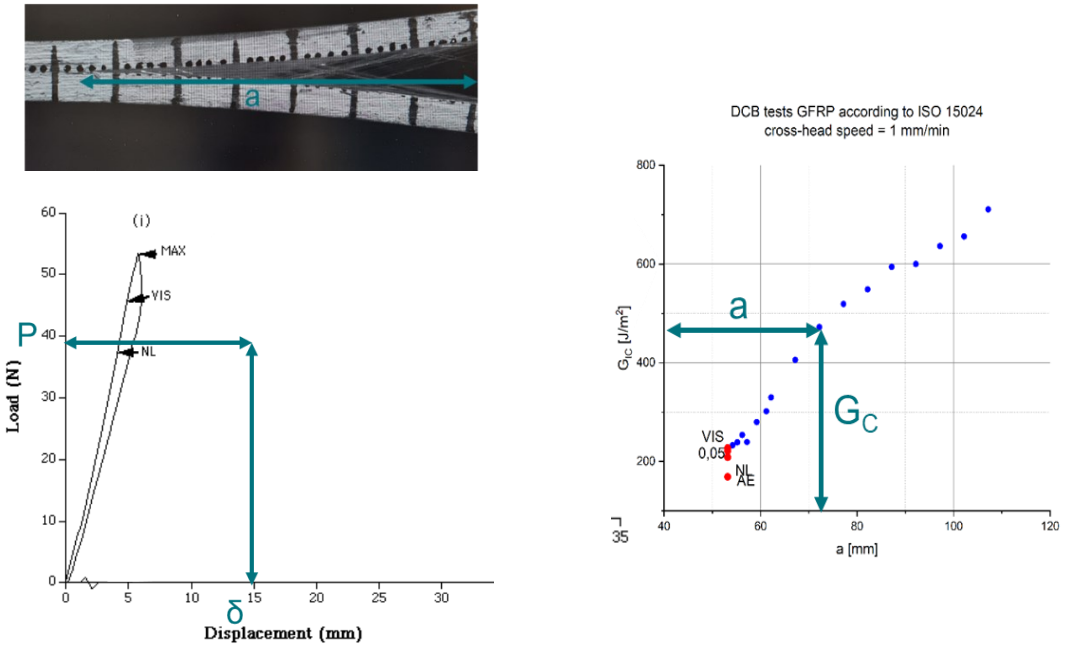


Figure 3.5: Optical determination of critical energy release rate.

## 3.4 Evaluation of fracture mechanical parameters

A complete resistance curve consists of the initiation and propagation values for the critical energy release rate. Therfore, the following will explain the evaluation of both.

### 3.4.1 Evaluation of delamination initiation

According to the standard methods, different initiation values can be determined. The Visual Onset (VIS), which shows the point when the crack starts to propagate, the point of deviation from linearity in the load-displacement curve (NL) and the point when the compliance has increased by 5 % or the load has reached its maximum (5%/max) [35]. In addition, a crack initiation value was established with the use of acoustic emission.

Therefore, a sudden increase of the cumulative absolute energy of the signals was defined as the onset point, as shown in Figure 3.6 b. As an example, Figure 3.6 a shows the onset points according to standard methods and by means of AE for a GFRP DCB specimen.

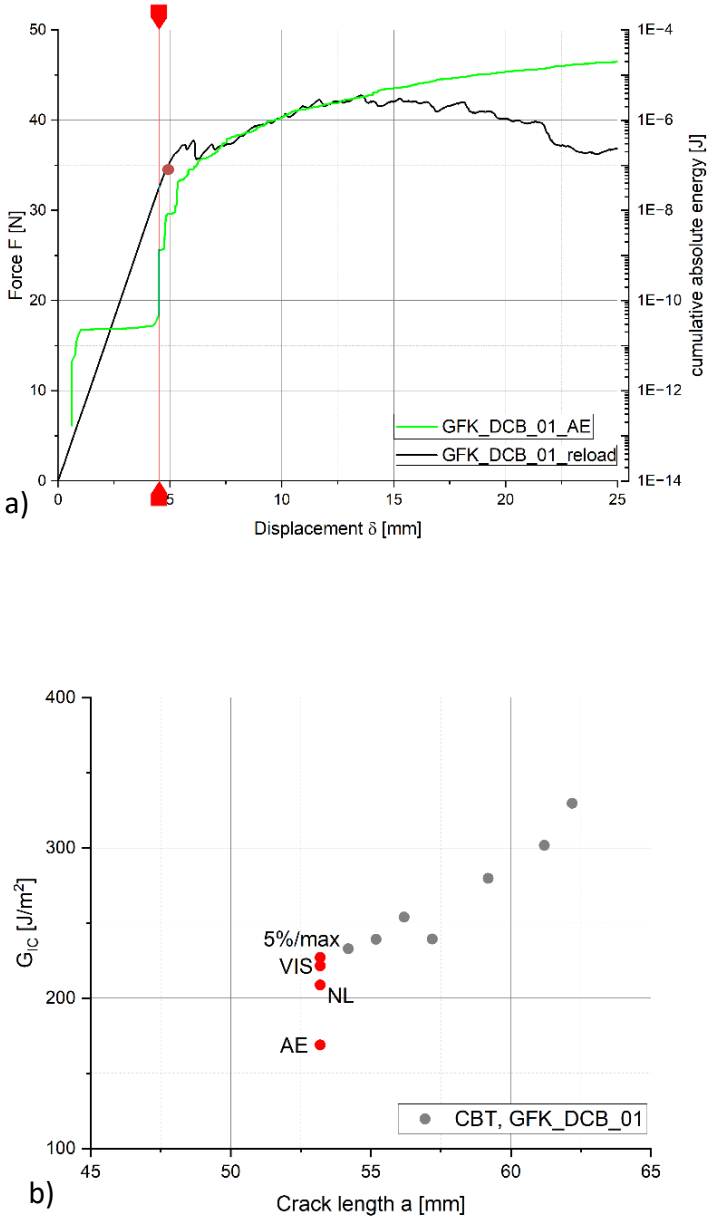


Figure 3.6: a) Onset points according to standard methods and by AE and b) determination of crack initiation with the use of AE.

### 3.4.2 Evaluation of delamination propagation

As already mentioned, in order to achieve the whole resistance curve the propagation values have to be determined as well. Therefore, the process described in 3.3.2 has to be applied to each increment of crack growth as shown in Figure 3.5.

# 4 RESULTS

## 4.1 Glass fiber reinforced polymer

The following shows the results of the GFRP laminate testing for all different tested configurations. For each setup, one force-displacement curve, one R-curve and a comparison of the crack front localization via AE and optically observed for one specimen are shown exemplary. The R-curve shows the initiation values for the energy release rate in red and the propagation points in black. Also, the R-curve is shown for different calculation methods according to each norm. The comparison of the localization of the crack front shows the results obtained via AE depending on the signal's amplitude in blue, green, and red and optically obtained in black. The results of all tested specimens can be found in the appendix.

### 4.1.1 Mode I – DCB

Figure 4.1 shows an exemplary force-displacement curve for mode I testing of GFRP. In Figure 4.2 the results for the energy release rate for that one specimen can be seen for the three calculation methods, that are described in the norm, beam theory (BT), corrected beam theory (CBT) and modified compliance calibration (MCC). While CBT and MCC give almost equal results, the energy release rates calculated by BT are higher compared to the other two methods. The R-curve does not lead in a plateau but keeps rising, which is a sign for fiber bridging. Figure 4.3 shows the results of the localization with both AE and optical observation. The optically observed crack front leads to a sharp curve, while AE yields a band of high amplitude signals around the crack front. This process zone can be explained by microscopic or macroscopic damage events occurring around the delamination front, like for example fiber bridging. Furthermore, the delamination length is not constant over the specimen width and therefore in any case would result rather in a band than in a straight line. Additionally, there is an uncertainty of localization resulting in scattering of the localized sources.

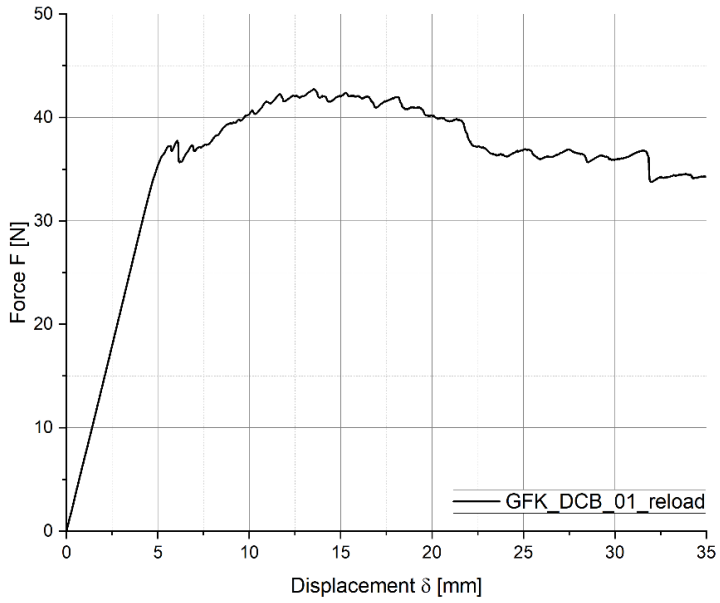


Figure 4.1: Force-displacement curve of a GFRP DCB test according to ISO 15024 - 01 (cross-head speed = 1 mm/min).

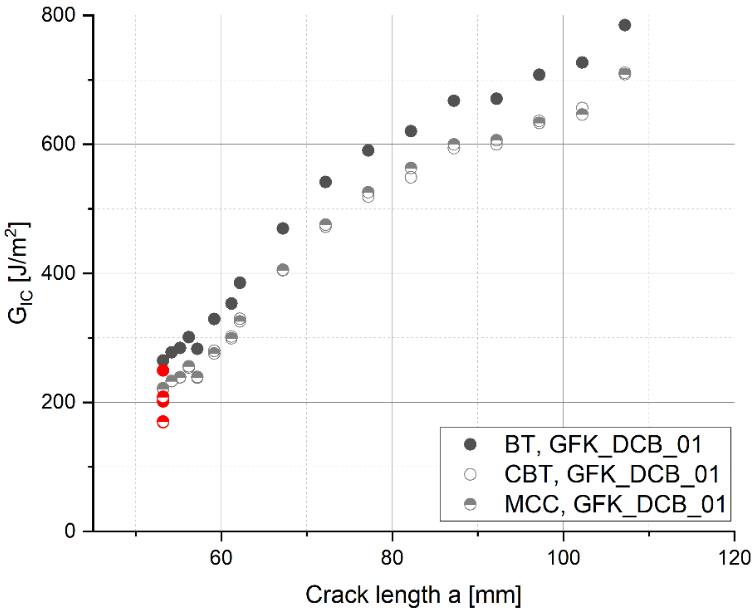


Figure 4.2 R-curve of a GFRP DCB test according to ISO 15024 - 01 (cross-head speed = 1 mm/min).

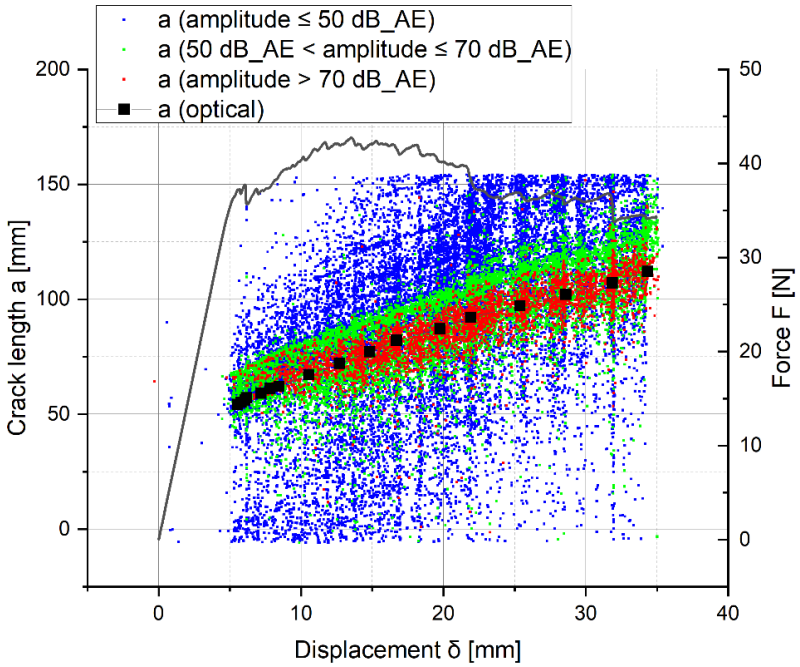


Figure 4.3: Comparison of AE source localization and optically observed crack front during a GFRP DCB test according to ISO 15024 - 01 (cross-head speed = 1 mm/min).

### 4.1.2 Mode II – ELS

Figure 4.4 shows an example of a force-displacement curve of an ELS test of a GFRP specimen. In Figure 4.5 the R-curves for the three calculation methods according to the norm, simple beam theory (SBT), experimental compliance method (ECM) and corrected beam theory using effective crack length (CBTE), can be seen. CBTE leads to the most conservative results, whereas SBT results in the least conservative. The energy release rates are approximately five times higher compared to mode I testing. Moreover, the R-curve results in a plateau. This is due to the fact that fiber bridging does not occur during mode II testing. Figure 4.6 shows the comparison of the crack front obtained optically and via AE. As for the DCB test the visually observed crack front correlates well with the high amplitude AE signals, even though the crack length does not grow linear over the displacement. The signals behind the crack front can be due to friction between the fracture surfaces during mode II testing.

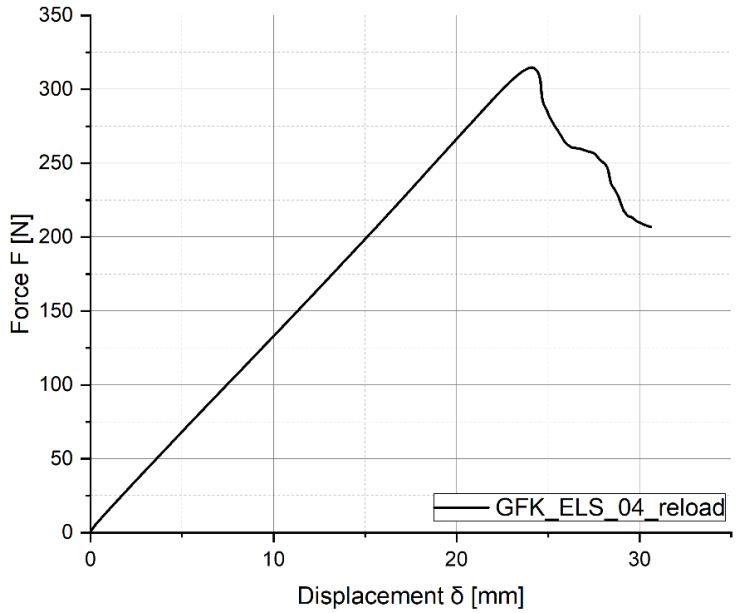


Figure 4.4: Force-displacement curve of a GFRP ELS test according to ISO/DIS 15114 – 12 (cross-head speed = 0,5 mm/min).

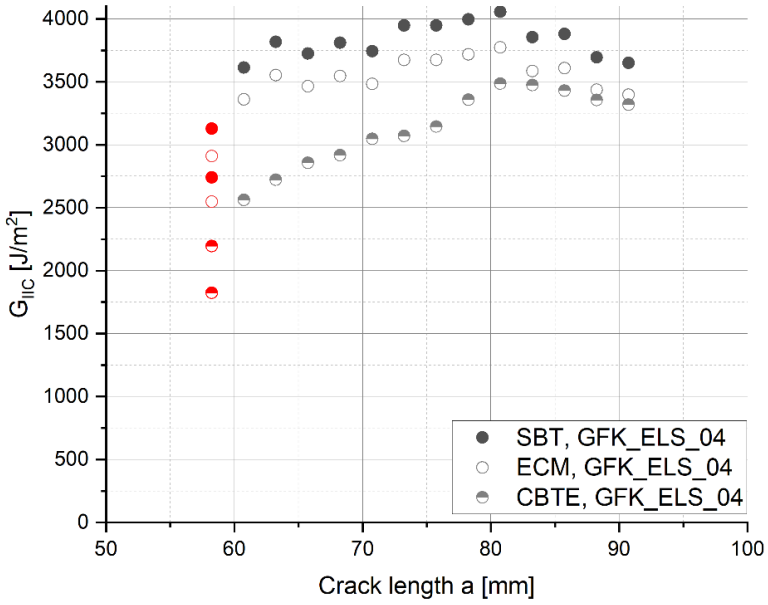


Figure 4.5: R-curve of a GFRP ELS test according to ISO/DIS 15114 - 12 (cross-head speed = 0,5 mm/min).

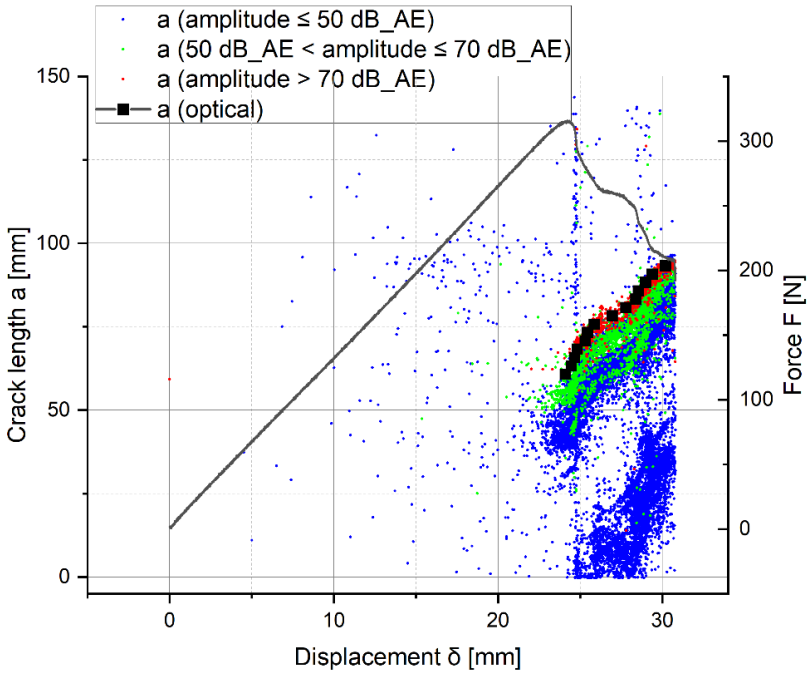


Figure 4.6: Comparison of AE source localization and optically observed crack front during a GFRP ELS test according to ISO/DIS 15114 - 12 (cross-head speed = 0,5 mm/min).

### 4.1.3 Mode II – ENF

Figure 4.7 shows the force-displacement curve of mode II ENF testing for one specimen. According to the norm, reloading has to be recorded as well, to calculate the crack length. Since the crack can only grow one increment in this configuration, only the crack initiation value can be determined with this test configuration, and therefore no R-curve can be obtained. The results of the initiation value with AE, NL value and the initiation value obtained from the one increment crack growth for the exemplary shown ENF test can be seen in Table 4. A crack front localization was not useful for this setup.

Table 4: Energy release rates of a GFRP ENF test according to ASTM D7905 – 14 (cross-head speed = 0,5 mm/min).

| | $G_{IIC}$ [J/m²] |
|---|---|
| **AE** | 1378 |
| **NL** | 1720 |
| **Initiation of Propagation** | 2285 |

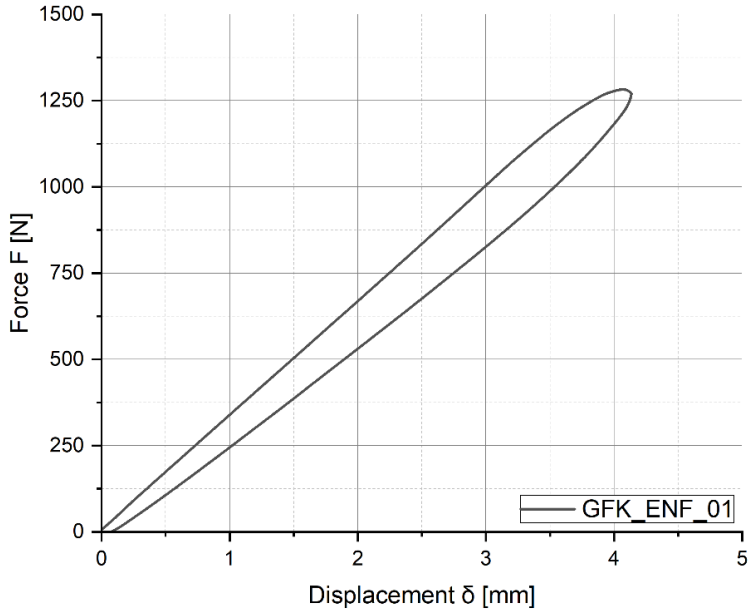


Figure 4.7: Force-displacement curve of a GFRP ENF test according to ASTM D7905 – 14 (cross-head speed = 0,5 mm/min).

### 4.1.4 Mixed mode I/II – FRMM

Figure 4.8 shows one force-displacement curve as an example of FRMM testing.

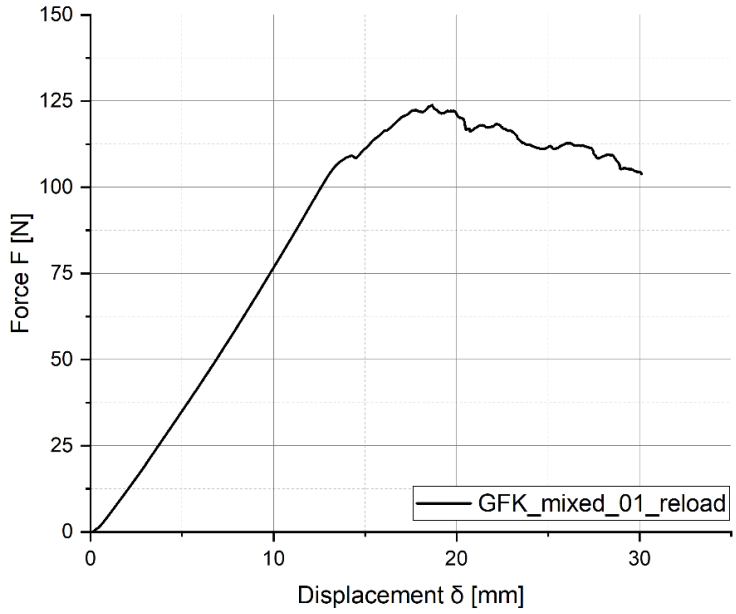


Figure 4.8: Force-displacement curve of a GFRP FRMM test according to ESIS TC4 Protocol (cross-head speed = 1 mm/min).

In Figure 4.9 the R-curve can be seen, which demonstrates all three calculation methods according to the norm. SBT has the highest values, while ECM shows the lowest values for the energy release rate. As for mode I testing, no plateau is achieved, due to fiber bridging

occurring during testing. The energy release rate values are between the values for mode I and mode II. Figure 4.10 shows that the visually observed crack front is in the zone of high amplitude AE signals.

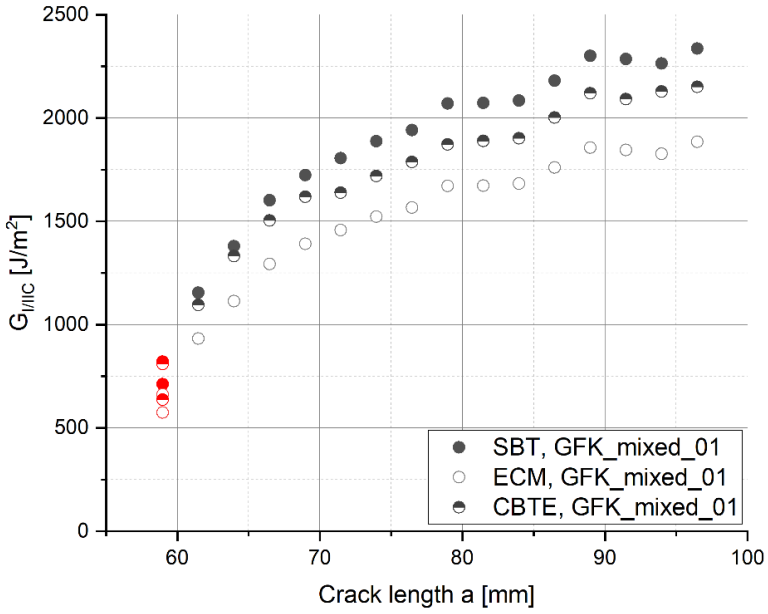


Figure 4.9: R-curve of a GFRP FRMM test according to ESIS TC4 Protocol (cross-head speed = 1 mm/min).

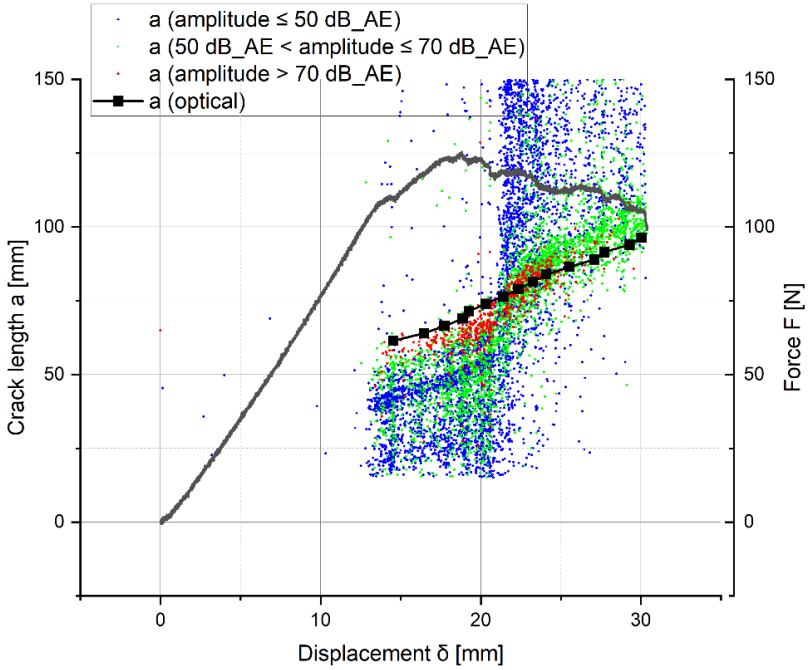


Figure 4.10: Comparison of AE source localization and optically observed crack front during a GFRP FRMM test according to ESIS TC4 Protocol (cross-head speed = 1 mm/min).

### 4.1.5 Mixed mode I/II – MMB

In Figure 4.11, one force-displacement curve for MMB testing can be seen. Figure 4.12 shows the corresponding R-curve with and without a lever weight correction. The R-curve for this setup did not show a plateau. The corrected values are slightly higher compared to the values without correction. For this setup only one sensor could be attached, therefore a localization was not possible.

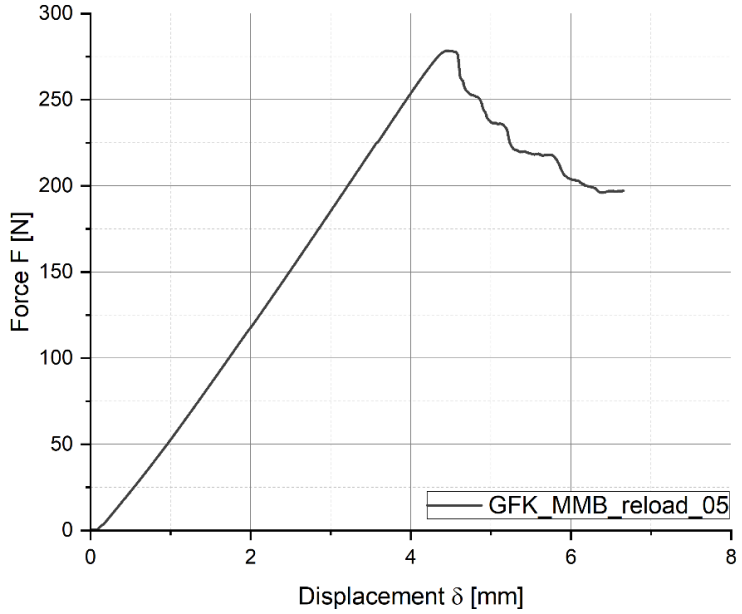


Figure 4.11: Force-displacement curve of a GFRP MMB test according to ASTM D6671 - 13 (cross-head speed = 0,5 mm/min).

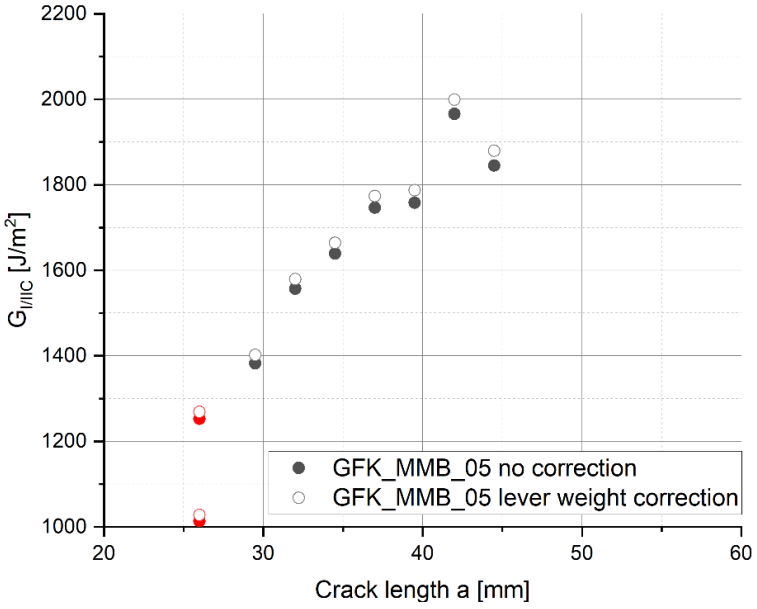


Figure 4.12: R-curve of a GFRP MMB test according to ASTM D6671 – 13 (cross-head speed = 0,5 mm/min).

### 4.1.6 Fracture surfaces

The following figures show the fracture surfaces of the GFRP laminate after testing with a magnification factor of 1000. A digital microscope of the type Keyence VHX-7000 (Keyence GmbH, Belgium) was used.

Figure 4.13 a) shows the fracture surface after mode I DCB testing. The fibers are evenly distributed with no loose matrix material between. The matrix fracture surfaces in between the fibers indicate brittle failure, appearing rather smooth and only showing slight unevenness. Figure 4.13 b) and c) show the fracture surfaces after mode II ELS and ENF testing, where shear hackles can be seen between the fibers, which is typical for mode II testing. In Figure 4.13 d) and e) the fracture surfaces after mixed mode I/II FRMM and MMB testing are shown. They do show shear hackles, but not as many as for pure mode II testing.

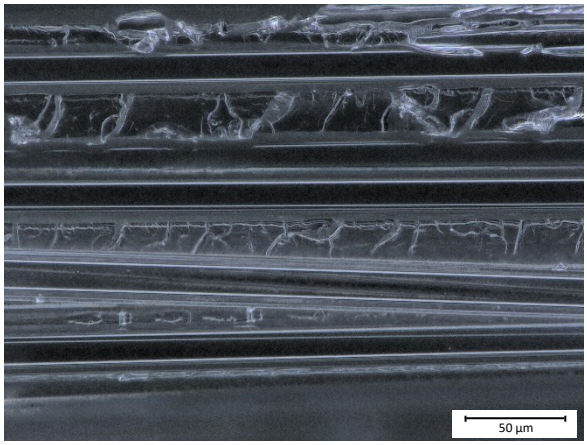


a)

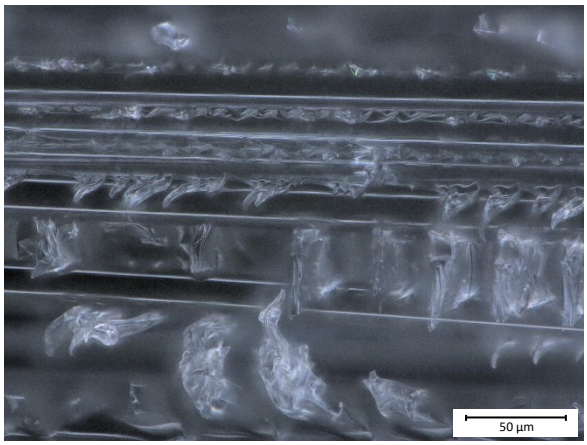


b)

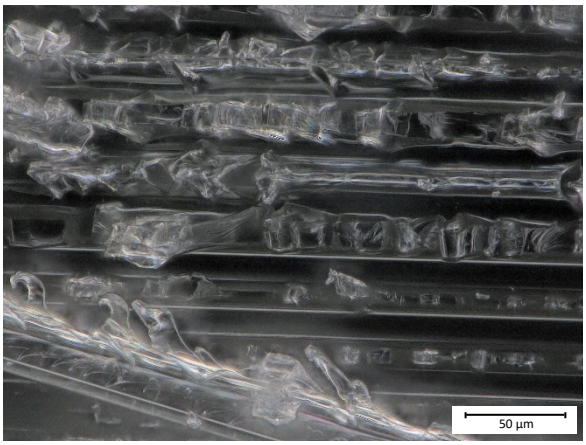


c)

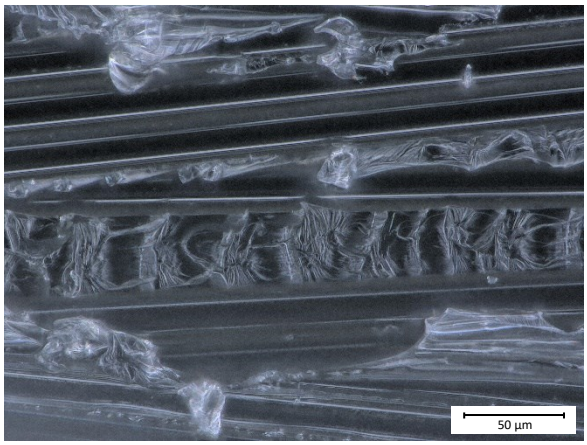


d)

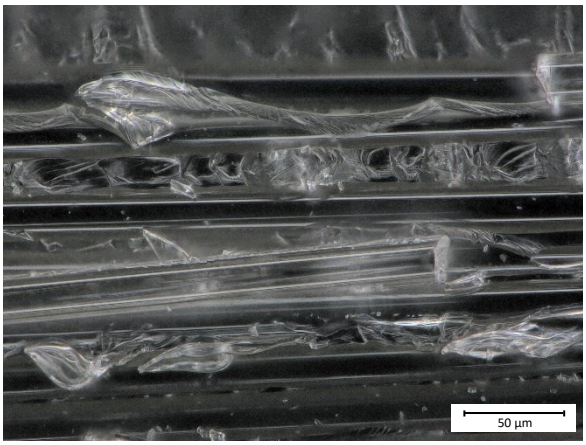


e)

Figure 4.13: Fracture surfaces of GFRP for a) mode I DCB, b) mode II ELS, c) mode II ENF, d) mixed mode I/II FRMM and e) mixed mode I/II MMB.

### 4.1.7 Summary of GFRP results

Figure 4.14 gives an overview of all results for all tested modes for GFRP. For each setup, an average of the results of all tested specimen was calculated in order to compare the results to each other. In orange the initiation value by means of AE and in green the initiation value determined from the non-linearity criterion, since this is the most conservative one, can be seen. The purple bar presents the average of the propagation values calculated with the compliance method. The compliance method was used since this method yielded in the most conservative results. For the calculation of the average of propagation, values after reaching a plateau in the resistance curve were included. If no plateau was formed in the resistance curve, values were taken from the point where a plateau could approximately be identified.

It can be seen that the initiation values are always smaller compared to the propagation values, and the onset obtained by AE is smaller than the onset of non-linearity for all setups, due to the sensitivity of AE and the objectivity of NL. Generally, it can be said that the critical energy release rate for mode I has the smallest value, mode II the highest and mixed mode I/II is in between. The critical energy release rate for mode II is almost seven times higher and for mixed mode I/II three times higher than for mode I. If the two methods for mode II, ELS and ENF, are compared, the initiation points for ENF are 30 % lower. If the two methods for FRMM and MMB are compared, FRMM yields results that are lower by approximately 45 %.

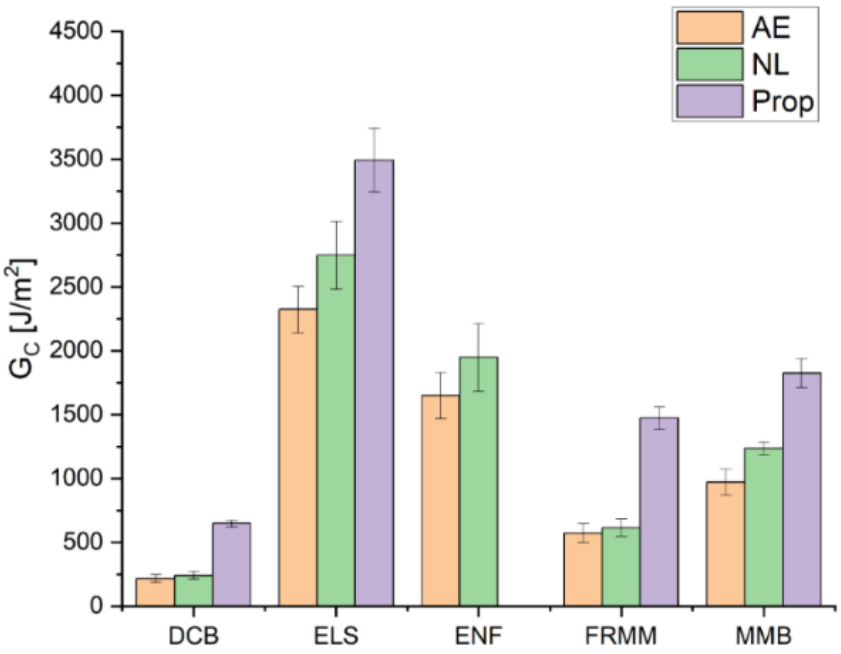


Figure 4.14: Results for all tested modes for GFRP.

## 4.2 Carbon fiber reinforced polymer

In the following the results of CFRP testing for all different configurations are presented. As for GFRP for each test setup one specimen's results are shown as an example and an overview of all results can be found in the appendix. For each setup a force-displacement curve, R-curve and the comparison of the crack front localization obtained optically and via AE are shown. In the R-curve the initiation values are presented in red and the propagation values in black. The color scheme for the crack front localization stays the same as well. The AE signals are presented in red, green, and blue according to their amplitude, while the visually observed crack front is shown in black.

### 4.2.1 Mode I – DCB

Figure 4.15 demonstrates a force-displacement curve for mode I DCB testing of a CFRP specimen and Figure 4.16 the corresponding results for the critical energy release rate. The results are shown for all three calculation methods that are mentioned in the standard method. While the results obtained with BT are the highest, CBT and MCC are equally smaller compared to BT. In Figure 4.17 the comparison of the localization of the crack front obtained via AE and optically are presented. The visually observed crack front is in the zone

of high amplitude AE signals. The process zone is rather narrow compared to the GFRP, which can be a result of less fiber bridging or the higher sound velocity in CFRP, leading to less scattering of the localized signals.

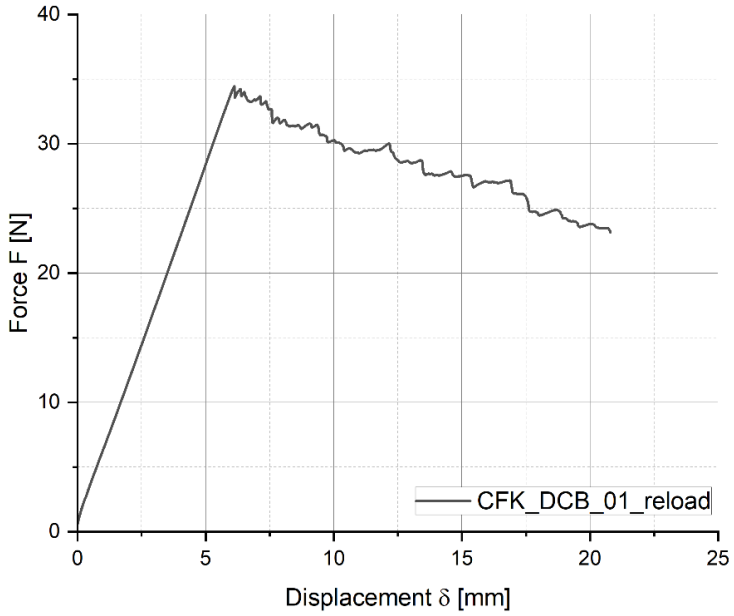


Figure 4.15: Force-displacement curve of a CFRP DCB test according to ISO 15024 - 01 (cross-head speed = 1 mm/min).

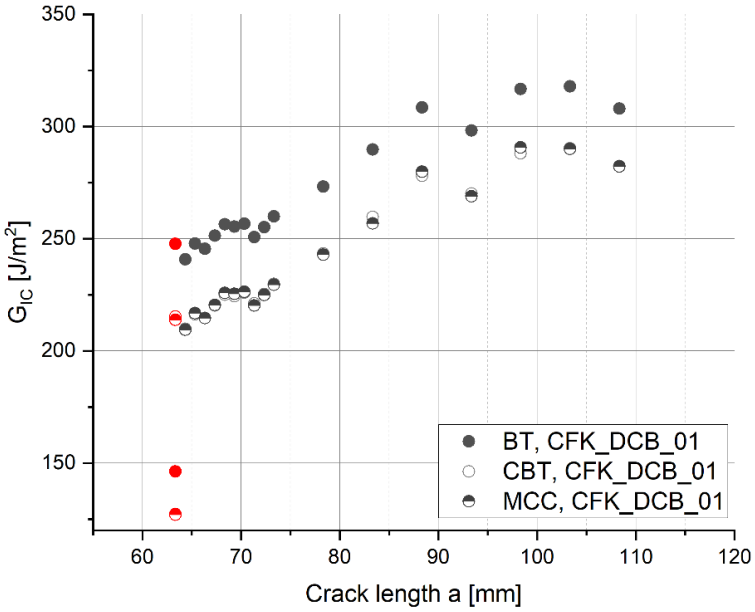


Figure 4.16 R-curve of a CFRP DCB test according to ISO 15024 - 01 (cross-head speed = 1 mm/min).

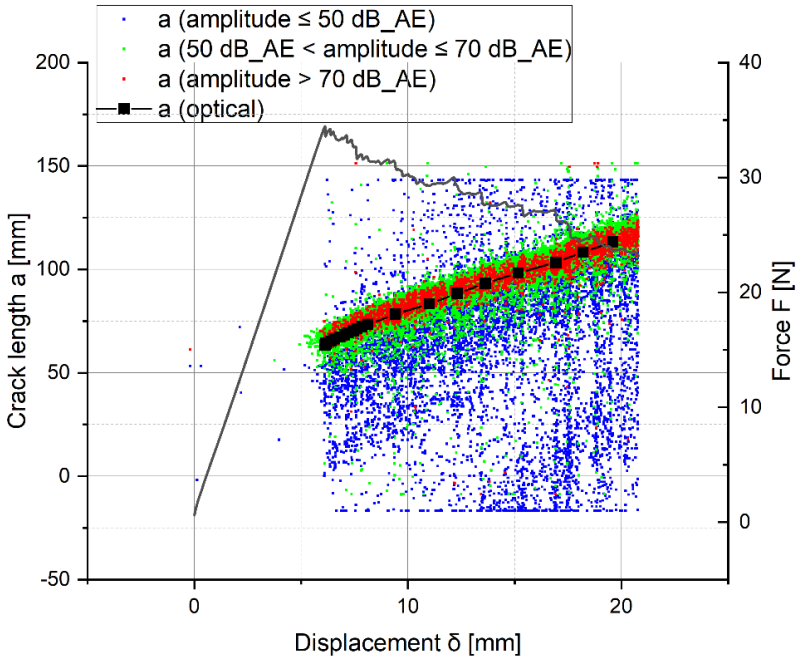


Figure 4.17: Comparison of AE source localization and optically observed crack front during a CFRP DCB test according to ISO 15024 – 01 (cross-head speed = 1 mm/min).

### 4.2.2 Mode II – ELS

In Figure 4.18, a force-displacement curve of a mode II ELS test is shown. Figure 4.19 presents the results for the critical energy release rate for the three calculation methods according to norm. The methods SBT and CBTE show similar results. ECM shows lower results compared to SBT and CBTE.

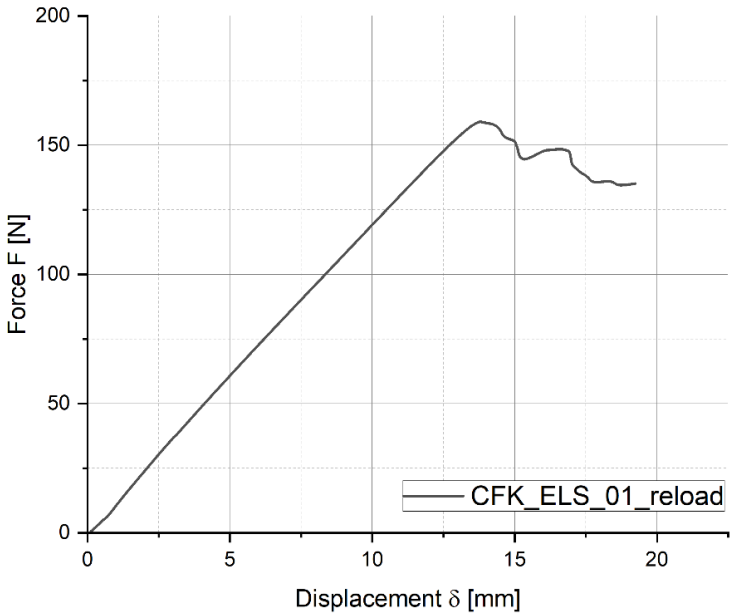


Figure 4.18: Force-displacement curve of a CFRP ELS test according to ISO/DIS 15114 – 12 (cross-head speed = 0,5 mm/min).

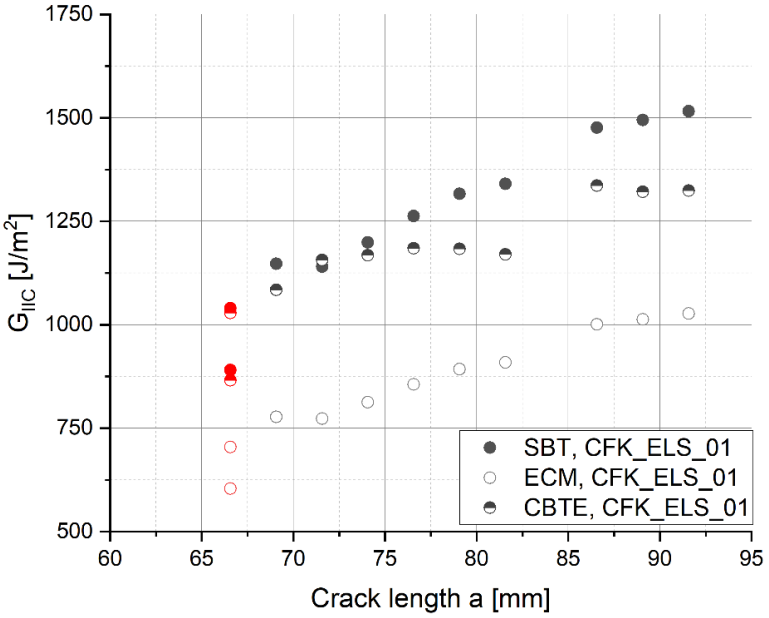


Figure 4.19: R-curve of a CFRP ELS test according to ISO/DIS 15114 - 12 (cross-head speed = 0,5 mm/min).

Figure 4.20 demonstrates the localization of the crack front. It can be noticed that the visually observed crack front lies within the zone of high energy AE signals. Figure 4.20 shows less signals behind the crack front compared to ELS results of GFRP laminates. This can be explained by a reduced surface roughness of the crack flanks in CFRP due to smaller shear hackles.

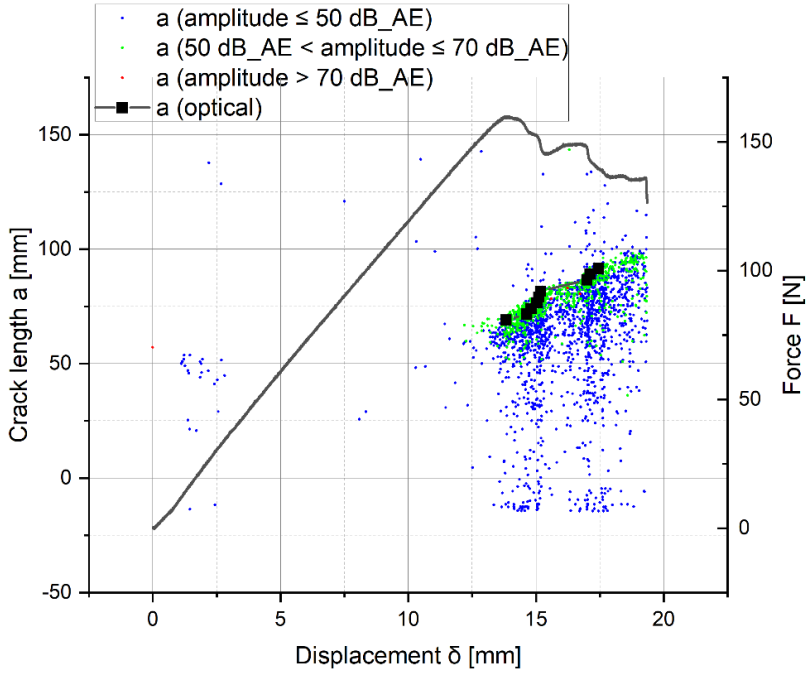


Figure 4.20: Comparison of AE source localization and optically observed crack front during a CFRP ELS test according to ISO/DIS 15114 - 12 (cross-head speed = 0,5 mm/min).

### 4.2.3 Mode II – ENF

In Figure 4.21, one force-displacement curve for mode II ENF testing is shown exemplary. As already mentioned before, only the crack initiation value can be determined with this test configuration since the crack only propagates one increment. Therefore, it is not possible to draw a resistance curve. The results of a CFRP ENF test can be seen in Table 5. A crack front localization was not useful for this setup.

Table 5: Energy release rates of a CFRP ENF test according to ASTM D7905 – 14 cross-head speed= 0,5 mm/min.

| | $G_{IIC}$ [J/m²] |
|---|---|
| **AE** | 831 |
| **NL** | 1016 |
| **Initiation of Propagation** | 1269 |

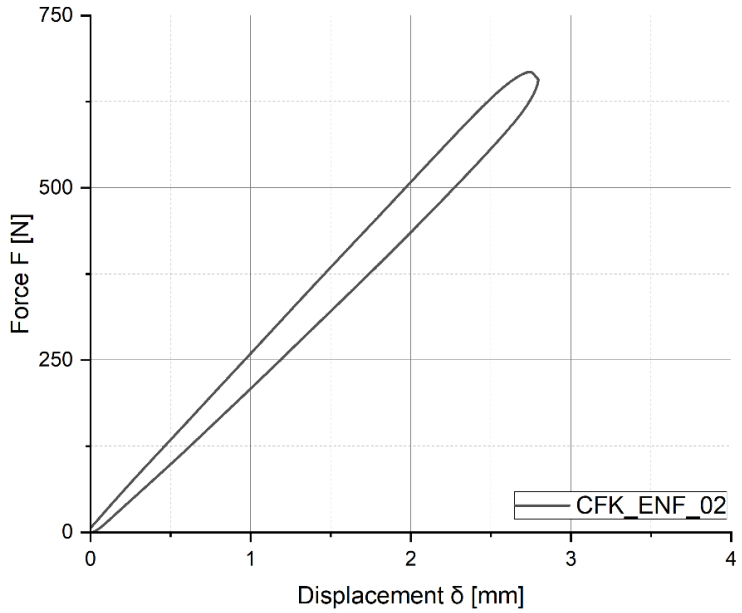


Figure 4.21: Force-displacement curve of a CFRP ENF test according to ASTM D7905 – 14 (cross-head speed = 0,5 mm/min).

### 4.2.4 Mixed mode I/II – FRMM

In Figure 4.22 a force-displacement curve for FRMM testing of CFRP is shown. Figure 4.23 presents the results for the critical energy release rate of this test configuration. According

to norm $G_{I/IIc}$ was calculated by three methods, SBT, ECM and CBTE. Figure 4.24 shows the results of the crack front localization. The visually observed crack front is in the zone of the highest amplitude AE signals in red.

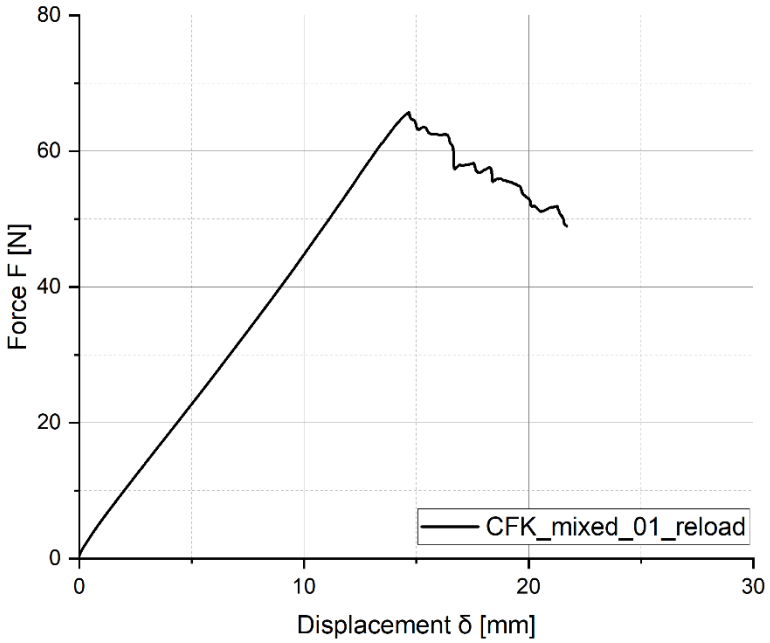


Figure 4.22: Force-displacement curve of a CFRP FRMM test according to ESIS TC4 Protocol (cross-head speed = 1 mm/min).

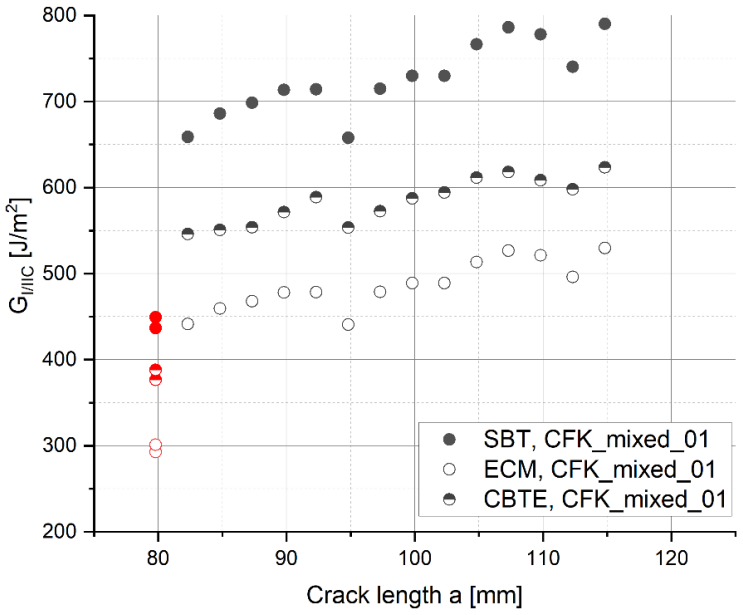


Figure 4.23: R-curve of a CFRP FRMM test according to ESIS TC4 Protocol (cross-head speed = 1 mm/min).

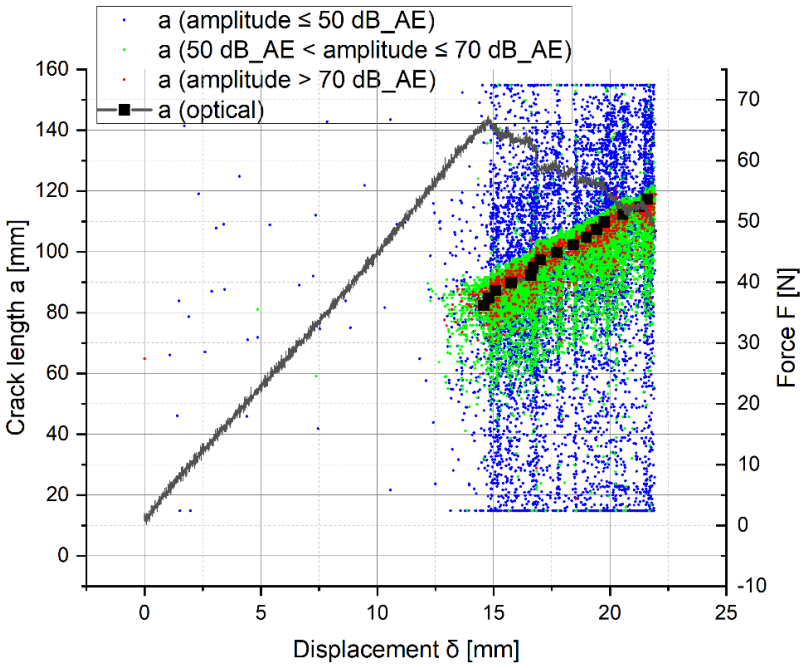


Figure 4.24: Comparison of AE source localization and optically observed crack front during a CFRP FRMM test according to ESIS TC4 Protocol (cross-head speed = 1 mm/min).

### 4.2.5 Mixed mode I/II – MMB

In Figure 4.25 a force-displacement curve for MMB testing can be seen. Figure 4.26 demonstrates the results for the critical energy release rate with and without a lever weight correction. The corrected results are slightly higher compared to the results without.

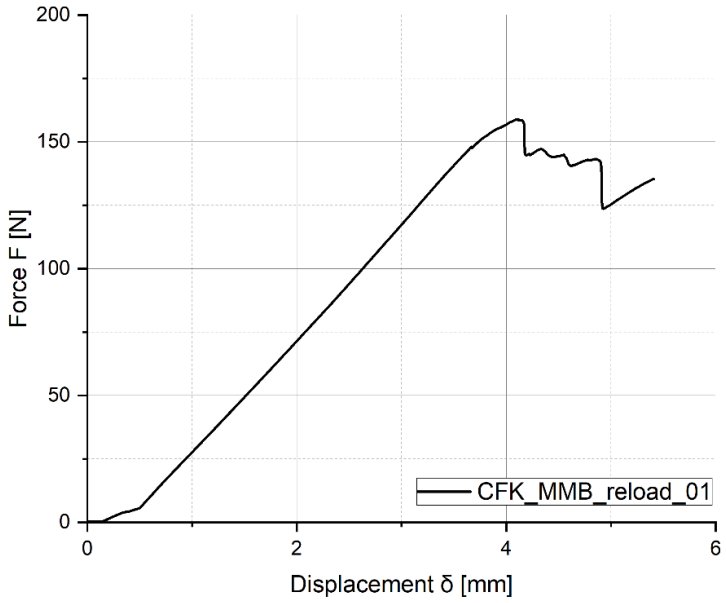


Figure 4.25: Force-displacement curve of a CFRP MMB test according to ASTM D6671 - 13 (cross-head speed = 0,5 mm/min).

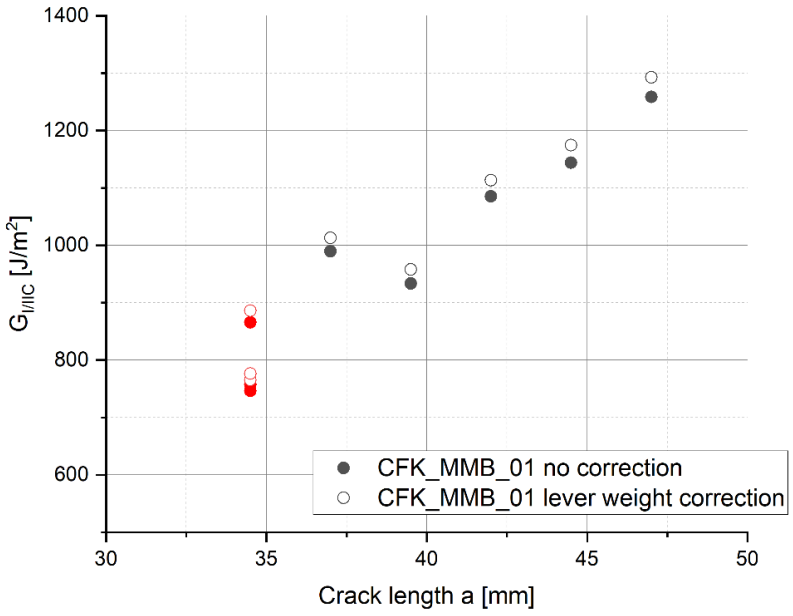


Figure 4.26: R-curve of a CFRP MMB test according to ASTM D6671 – 13 (cross-head speed = 0,5 mm/min).

### 4.2.6 Fracture surfaces

The following figures show the fracture surfaces of CFRP after each different tested mode at a magnification factor of 1000. A digital microscope of the type Keyence VHX-7000 (Keyence GmbH, Belgium) was used.

Figure 4.27 a) presents the surface of a CFRP specimen after mode I DCB testing. The fibers are evenly distributed with no loose matrix material between. The matrix fracture surfaces are smooth only showing a slight unevenness, indicating brittle fracture. In Figure 4.27 b) and c), the surfaces after mode II ELS and ENF testing are presented, showing shear hackles between the fibers, which is typical for mode II testing. In Figure 4.27 d) and e) the surfaces after mixed mode I/II FRMM and MMB testing can be seen. The surfaces depict some shear hackles between the fibers, but in general appears more regular compared to pure mode II. These results are in accordance with the results presented in the PhD thesis of Cvitkovich. He presents the fracture surfaces of mode I, II and mixed mode I/II tests of a CFRP laminate and also comes to the result that mode II and mixed mode I/II show shear hackles, while mode I does not [13].

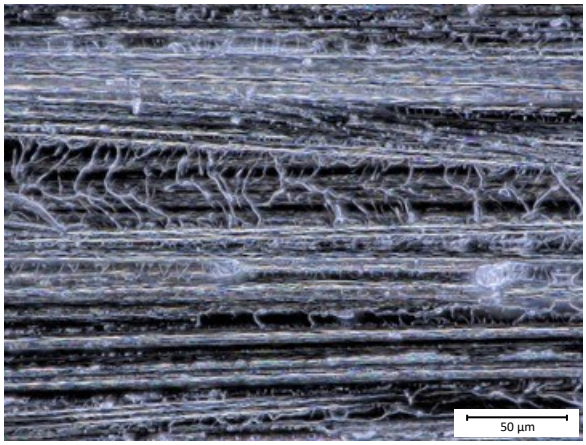


a)

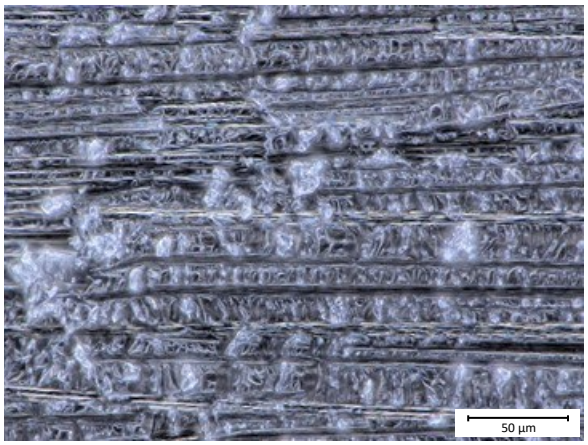


b)

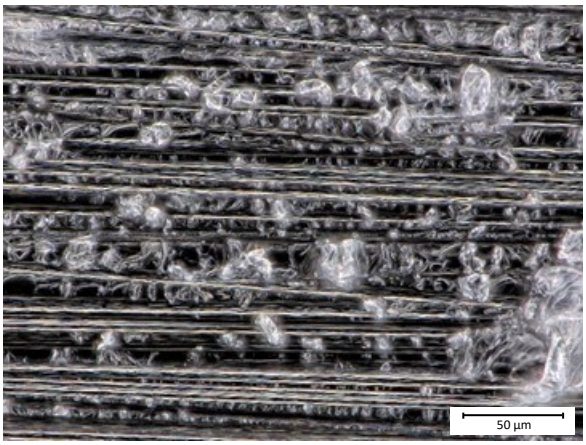


c)

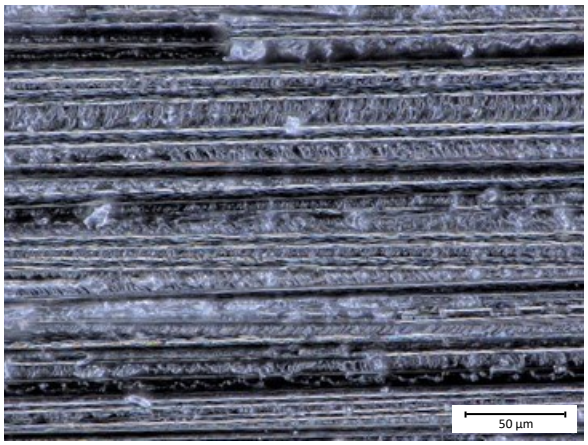


d)

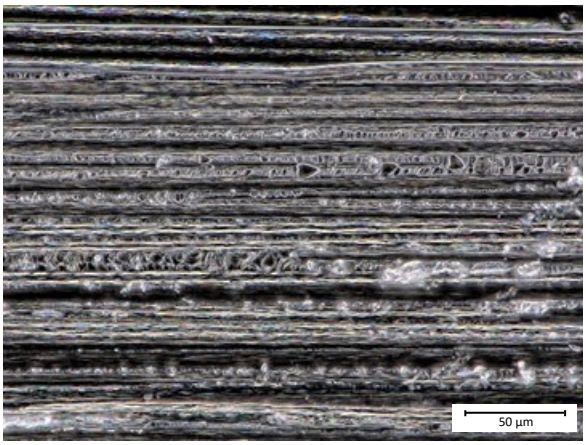


e)

Figure 4.27: Fracture surfaces of CFRP for a) mode I DCB, b) mode II ELS, c) mode II ENF, d) mixed mode I/II FRMM and e) mixed mode I/II MMB.

### 4.2.7 Summary of CFRP results

Figure 4.28 presents the results of all tested specimen for all test configurations. In order to compare the results to each other, an average of all tested specimen for each test setup was calculated. In orange, the average of the initiation values obtained by AE and in green, the initiation values determined from the non-linearity criterion can be seen. In purple, the average of the propagation values is presented. To calculate the average propagation value, the compliance calibration method results were used, since they yield the most conservative results. Additionally, only values after reaching a plateau were considered. If no plateau was formed, values were taken from the point where a plateau could approximately be identified.

The values for initiation are smaller compared to the propagation values, and the AE onset is the most conservative one. In general, it can be said that the critical energy release rate for mode I is the smallest, for mode II the highest and mixed mode I/II is in between. The critical energy release rate for mode II is five times higher and for mixed mode I/II three times higher than for mode I.

If the two mode II test methods, ELS and ENF, are to be compared, it can be noticed that the ENF initiation points are as high as the propagation values of ELS. $G_{I/IIc}$ of FRMM is smaller than MMB by approximately 48%.

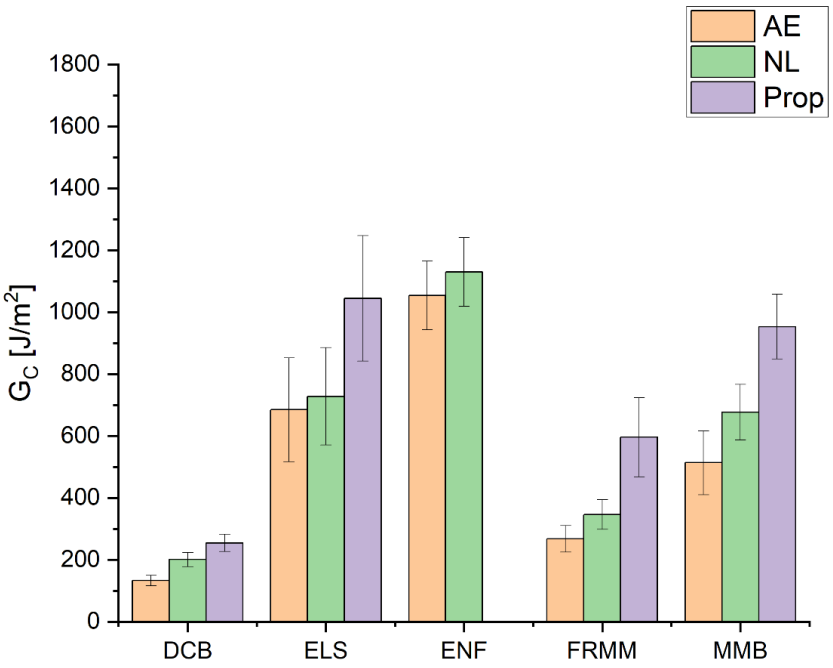


Figure 4.28: Results for all tested modes for CFRP.

## 4.3 Comparison of GFRP and CFRP

In the following the results of GFRP and CFRP are compared to each other. Looking at the localization results of DCB testing for both materials in Figure 4.3 and Figure 4.17, it can be noticed that the band with high amplitude AE signals is wider for GFRP compared to CFRP. This could be a result of fiber bridging, which was stronger pronounced in GFRP tests, as can be seen in Figure 4.29. Since fiber bridging leads to a resistance curve without a plateau, this effect is also noticeable when comparing the resistance curves of GFRP (Figure 4.2) and CFRP (Figure 4.16) for mode I testing. While the curve of GFRP does not show a plateau, the curve of CFRP does. The same effect can be seen for FRMM testing. The resistance curve for GFRP in Figure 4.9 does not show a plateau, while the curve of CFRP in Figure 4.23 does. Another reason for the wider distributed AE signals for GFRP laminates is that the velocity of sound in a certain material has an impact on the scatter of the signals. Since GFRP has a lower sound velocity compared to CFRP laminates, the localization is less accurate. Also, in GFRP laminates AE signals can be detected at low loads, while in CFRP laminates it often takes a higher load to detect the first signal.

While established approaches, such as IR or optical methods, often suffer from low accuracy, crack tip localization based on AE correlated well with the visually observed crack front.

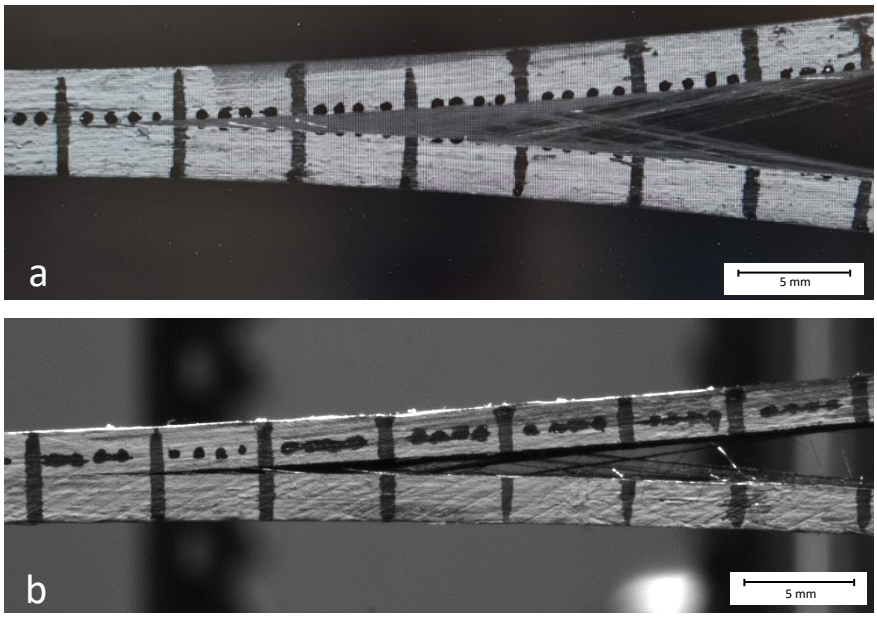


Figure 4.29: Fiber bridging of a a) GFRP and b) a CFRP specimen during DCB testing.

Having a look at the overview of all results in Figure 4.30, it can be said that both materials show the same trends. For both GFRP and CFRP, the initiation values are lower than the propagation values. Furthermore, the initiation values obtained by AE are more conservative compared to the onset determined by the non-linearity criterion. This has already been proposed by Sause et al., when they compared different onset criteria with onset values obtained with AE. They concluded that the onset obtained by AE can be used as a criterion to detect the first onset of microscopic damage and that this criterion is in the range of the start of a non-linear force-displacement curve [30]. The energy release rate is the lowest for mode I, the highest for mode II and for mixed mode I/II the rate is between mode I and II for GFRP and CFRP. This is in accordance with the work of Kinloch and Williams, which showed the same trend for mode I, II and mixed mode I/II for carbon fiber composite materials [36]. The values for GFRP are approximately double the values for CFRP. This can be due to various reasons. Since both fibers are embedded in the same matrix system, it can be due to different fiber-matrix adhesion. Another reason could be the different dimensions of the fiber types. The two different setups for mode II testing, ELS and ENF, show different trends for the two materials. While ELS yields higher results

for the energy release rate than ENF for GFRP, the CFRP shows the opposite trend. The results for CFRP are in accordance with the work of Davies et al. They compared different test configurations for mode II testing for CFRP and concluded that ENF shows slightly higher results than ELS [37]. Comparing the two methods for mixed mode I/II testing, FRMM and MMB, both laminates exhibit slightly higher results for MMB than FRMM.

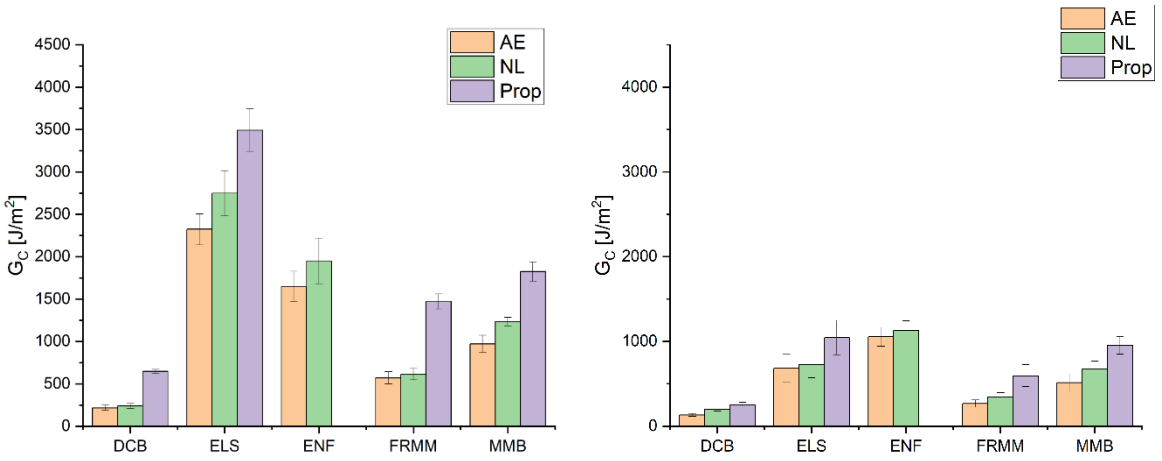


Figure 4.30: Comparison of results of GFRP and CFRP.

The fracture surfaces show similar results for GFRP and CFRP as well. The results are also in accordance with the research of Abd Rased and Yoon. In their work they showed Scanning electron microscope images of DCB, ENF and MMB tests. The DCB images showed typical effects for mode I, such as brittle matrix cleavage and flat fiber imprints. The images of ENF and MMB tests showed typical effects for mode II like hackle and cusp formations. The main difference between fracture surfaces of different modes is the hackle formation, which occurs more often with an increasing mode II ratio [38].

# 5 CONCLUSION AND OUTLOOK

The focus of this work was to determine the critical energy release rate of GFRP and CFRP laminates for mode I, II and mixed mode I/II. Moreover, the critical energy release rate for mode II and mixed mode I/II was obtained according to two different standard methods each. The results for the different modes and for the same mode, but tested with different configurations, were to be compared. Furthermore, the onset and propagation of delamination was not only evaluated according to the standard methods, but also via AE.

The determination of the critical energy release rate for all tested modes for both materials showed similar trends. The initiation values were lower than the propagation values. Moreover, the initiation values determined with AE onset resulted in the most conservative critical energy release rates, followed by the initiation value determined at the point of non-linearity in the force-displacement curve. This showed that AE can be a feasible method to determine the onset of delamination, especially because it is not as error-prone compared to the determination of initiation at non-linearity, as has been shown in the round robin testing resulting in a coefficient of variation of 5 % [7].

Furthermore, the critical energy release rate for GFRP was approximately two times higher than for CFRP, which can be due to various reasons. Both fibers were embedded in the same matrix system, therefore it can be due to different fiber-matrix adhesion. Another reason could be the different dimensions of the two fiber types.

Moreover, both materials showed the same trend of the critical release rate of the different modes tested. For GFRP and CFRP, mode I resulted in the lowest values of $G_C$. Mode II testing showed the highest values for the critical energy release rate and the results of mixed mode I/II were between those for mode I and II.

The fracture surfaces showed differences depending on the tested mode. The surfaces after mode I testing showed evenly distributed fibers with no loose matrix material between. The matrix fracture surfaces were smooth only showing a slight unevenness, indicating brittle fracture. Mode II surfaces showed shear hackles, which is a typical phenomenon for this mode of testing. On the fracture surfaces of specimens tested under mixed mode I/II, evenly distributed fibers and shear hackles could both be seen.

The localization via AE yielded good results in accordance with the optically obtained crack front, which could be seen in a band of high amplitude AE signals around the optically observed crack front. This band seemed to be wider for GFRP compared to CFRP. This can be explained by fiber bridging, which occurred more pronounced in GFRP. This explanation could be confirmed by the resistance curve of both materials. The R-curve of CFRP showed a plateau, while the curve for GFRP did not, which is another sign for strong fiber bridging. Another reason for the wider distributed signals for GFRP could be the lower sound velocity in GFRP compared to CFRP which yields in a lower accuracy of signal localization.

In conclusion, it can be said that the tested methods had consistent results and both materials showed the same trends. AE proved to be a helpful method for the determination of delamination behavior of composite materials. AE can be applied both to determine the onset of delamination and to localize the crack front. With the use of AE, results can be obtained objectively and with less personal error compared to other methods.

# 6 REFERENCES

[1] H. Schürmann, Konstruieren mit Faser-Kunststoff-Verbunden, second ed., Springer, Berlin, 2007.

[2] M. Knops, Analysis of Failure in Fiber Polymer Laminates: The Theory of Alfred Puck, Springer, Heidelberg, 2008.

[3] D.K. Rajak, D.D. Pagar, P.L. Menezes, E. Linul, Fiber-Reinforced Polymer Composites: Manufacturing, Properties, and Applications, Polymers (2019) 1667.

[4] J. Geier, Methods for automated crack length detection in fracture mechanical fatigue tests of unreinforced polymers. Mastarbeit, Leoben, 2019.

[5] Ziehl, P., Pollock, A. (Ed.), Acoustic Emission, IntechOpen, Rijeka, 2012.

[6] Grosse, C. U., Ohtsu, M., Acoustic Emission Testing: Basics for Research - Application in Civil Engineering, Springer, Berlin, 2008.

[7] P. Davies, Round Robin Analysis of GIc Interlaminar Fracture Test, Applied Composite Materials (1996) 135–140.

[8] AVK - Industrievereinigung Verstärkte Kunststoffe, Handbuch Faserverbundkunststoffe/ Composites: Grundlagen, Verarbeitung, Anwendungen, Springer Vieweg, Wiesbaden, 2014.

[9] Ativitavas, N., Pothisiri, T. and Fowler, T. J., Identification of Fiber-reinforced Plastic Failure Mechanisms from Acoustic Emission Data using Neural Networks, Composite Materials (2006).

[10] R. Khan, Fiber bridging in composite laminates: A literature review, Composite Structures (2019).

[11] S. Sridharan, Delamination behaviour of composites, Woodhead Publishing Limited, Cambridge, 2008.

[12] H. Schmiedel, Handbuch der Kunststoffprüfung, Karl Hanser Verlag, München, 1992.

[13] M. Cvitkovich, “Polymer Matrix Effects On Interlaminar Crack Growth In Advanced Composites Under Monotonic And Fatigue Mixed-Mode I/II Loading Conditions. Dissertation, Leoben, 1995.

[14] Grellmann, W., Seidler, S., Polymer Testing, second ed., Carl Hanser Verlag GmbH & Co. KG, 2013.

[15] A. Gosch, Polymer fracture mechanics extended to large plastic deformation and mixed mode loading. Dissertation, Leoben, 2021.

[16] T.L. Anderson, Fracture Mechanics fundamentals and applications, CRC Press, Florida, 1991.

[17] Williams, J. G., Moore, D. R., Pavan, A., Fracture Mechanics Testing Methods for Polymers Adhesives and Composites, Elsevier Science Ltd, Oxford, 2001.

[18] N. Perez, Fracture Mechanics, Kluwer Academic Publishers Group, Dordrecht, 2004.

[19] Ewalds, H. L., Wanhill, R. J. H., Fracture Mechanics, Edward Arnold, London, 1984.

[20] R.W. Hertzberg, Deformation and Fracture Mechanics of Engineering Materials, John Wiley & Sons Inc., USA, 1996.

[21] Schuecker, C., Davidson, B. D., Evaluation of the accuracy of the four-point bend end-notched ¯exure test for mode II delamination toughness determination, Composites Science and Technology (2000) 2137–2146.

[22] Brunner, A. J., Blackman, B. R. K., Davies, P., A status report on delamination resistance testing of polymer–matrix composites, Engineering Fracture Mechanics (2008) 2779–2794.

[23] B. Blackman, Determination of the Mixed-Mode I/II Delamination Resistance of Unidirectional Fibre-Reinforced Polymer Laminates Using the Asymmetric Double Cantilever Beam Specimen (ADCB), 2015.

[24] M.G.R. Sause, In Situ Monitoring of Fiber-Reinforced Composites: Theory, Basic Concepts, methods, and Applications, Springer, Augsburg, 2016.

[25] P.J. Groot, P.A.M. Wijnen, Janssen R. B. F., Real-time frequency determination of acoustic emission for different fracture mechanisms in carbon/epoxy composites, Composites Science and Technology (1995) 405–412.

[26] M. Eaton, K. Holford, F. Carol, R. Pullin, An investigation of frequency as an acoustic emission signal discriminator in carbon fivre composite materials, 6th International Conference on Acoustic Emission (2007).

[27] J.R. Matthews, Acoustic Emission: Nondestructive Testing Monographs and Tracts, second ed., Gordon and Breach Science Publishers Ltd., New York, 1983.

[28] R. Unnþórsson (Ed.), Acoustic Emission: Research and Applications, IntechOpen, Rijeka, 2012.

[29] P.A. Tipler, G. Mosca, Physik für Wissenschaftler und Ingenieure, seventh ed., Springer, Heidelberg, 2015.

[30] A.J. Brunner, Identification of damage mechanisms in fiber-reinforced polymer-matrix composites with Acoustic Emission and the challenge of assessing structural integrity and service-life, Construction and Building Materials (2018) 629–637.

[31] A.J. Brunner, Correlation between acoustic emission singals and delaminations in carbon fiber-reinforced polymer-matrix composites: A new look at mode I fracture test data, Czech Society for Non-destructive Testing (2016) 55–63.

[32] Sause, M. G. R., Müller, T., Horoschenkoff, A., Horn, S., Quantification of failure mechanisms in mode-I loading of fiber reinforced plastics utilizing acoustic emission analysis, Composites Science and Technology (2012) 167–174.

[33] S. Stelzer, Optimized experimental methods for the description of the delamination and failure behavior of high performance composites and joints. Dissertation, Leoben, 2014.

[34] Physical Acoustics Corporation, PCI-2-Based AE system: User's Manual, 2007.

[35] Standard Test Method for Mode I Interlaminar Fracture Toughness of Unidirectional Fiber-Reinorced Polymer Matrix Composites, 2013.

[36] Kinloch, A. J., Williams, J. G., Delamination Fracture of Multidirectional Carbon-Fiber/Epoxy Composites under Mode I, Mode II and Mixed-Mode I/II Loading, Journal of Composite Materials (1999) 73–100.

[37] P. Davies, G.D. Sims, P. Davies, G. D. Sims, B. R. K. Blackman, A. J. Brunner, K. Kageyama, M. Hojo, K. Tanaka, G. Murri, C. Rousseau, B. Gieseke, R. H. Martin, Comparison of test configurations for the determination of Giic results from an international round robin, Plastics, Rubber and Composites (1999) 432–437.

[38] M.F. Abd Rased, S.H. Yoon, Experimental study on effects of asymmetrical stacking sequence on carbon fiber/epoxy filament wound specimens in DCB, ENF, and MMB tests, Composite Structures (2021).

# 7 APPENDIX

## 7.1 GFRP

Table 6: Overview of all GFRP results, obtained from average values of all calculation methods according to each norm.

| | | | AE [J/m²] | NL [J/m²] | VIS [J/m²] | 5 % / max [J/m²] | Propagation [J/m²] |
|---|---|---|---|---|---|---|---|
| **DCB** | **BT** | **Average** | 253,71 | 283,11 | 296,94 | 303,53 | 716,19 |
| | | **Deviation** | 33,40 | 28,20 | 26,23 | 28,45 | 20,67 |
| | **CBT** | **Average** | 214,53 | 239,56 | 251,12 | 256,74 | 646,76 |
| | | **Deviation** | 30,51 | 28,84 | 27,15 | 29,45 | 25,73 |
| | **MCC** | **Average** | 213,61 | 238,31 | 247,83 | 251,76 | 645,71 |
| | | **Deviation** | 29,28 | 28,81 | 25,90 | 27,82 | 25,98 |
| **ELS** | **SBT** | **Average** | 2485,94 | 2838,03 | 2916,73 | 3109,03 | 3677,96 |
| | | **Deviation** | 212,32 | 314,31 | 355,30 | 316,93 | 279,26 |
| | **ECM** | **Average** | 2321,95 | 2689,64 | 2760,54 | 2945,71 | 3491,52 |
| | | **Deviation** | 181,51 | 255,67 | 264,89 | 238,86 | 248,50 |
| | **CBTE** | **Average** | 2242,57 | 2808,82 | 2864,75 | 3345,87 | 3651,20 |
| | | **Deviation** | 285,17 | 592,67 | 529,91 | 453,41 | 324,06 |
| **ENF** | | **Average** | 1648,25 | 1947,60 | | | 2606,00[1] |
| | | **Deviation** | 216,83 | 199,64 | | | 218,80[1] |
| **FRMM** | **SBT** | **Average** | 690,24 | 741,52 | 939,66 | 945,48 | 1784,32 |
| | | **Deviation** | 72,02 | 53,51 | 166,82 | 158,75 | 80,81 |

[1] Initiation of propagation

| | | | | | | | |
|---|---|---|---|---|---|---|---|
| | **ECM** | **Average** | 570,55 | 613,36 | 780,63 | 785,37 | 1472,23 |
| | | **Deviation** | 73,43 | 66,37 | 166,60 | 160,62 | 87,86 |
| | **CBTE** | **Average** | 661,37 | 753,59 | 991,42 | 1063,69 | 1676,82 |
| | | **Deviation** | 27,02 | 38,75 | 181,09 | 178,27 | 73,23 |
| **MMB** | **No Corr.** | **Average** | 970,33 | 1233,50 | 1295,80 | 1302,54 | 1823,77 |
| | | **Deviation** | 103,42 | 50,43 | 60,27 | 60,26 | 114,86 |
| | **Lever weight Corr.** | **Average** | 985,14 | 1250,22 | 1312,92 | 1319,71 | 1853,10 |
| | | **Deviation** | 103,69 | 50,39 | 60,34 | 60,28 | 115,94 |

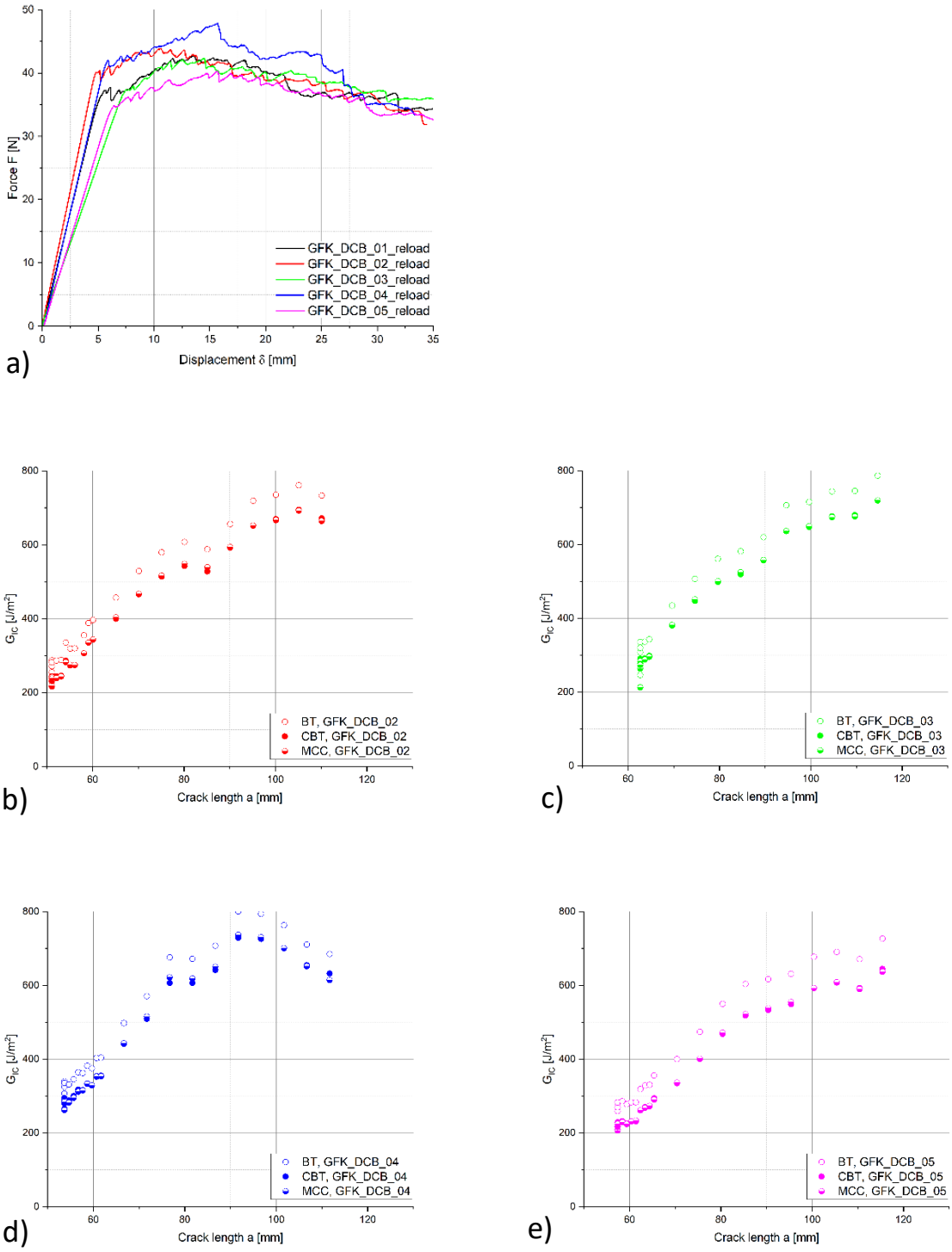


Figure 7.1: a) Force-displacement curve and b)-e) R-curves of GFRP DCB tests according to ISO 15024 (cross-head speed = 1 mm/min).

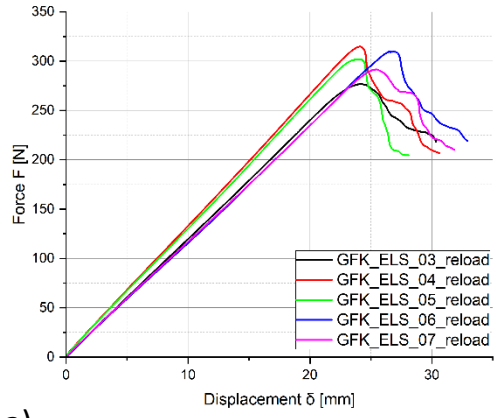


a)

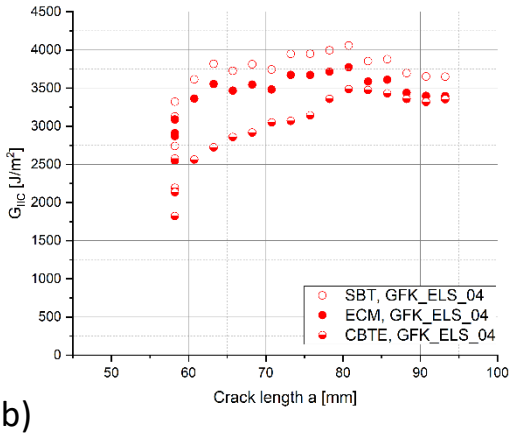


b)

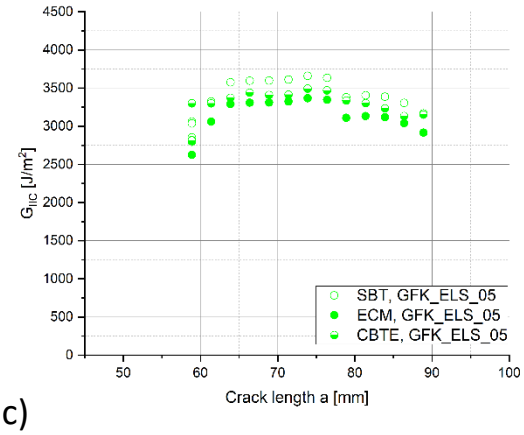


c)

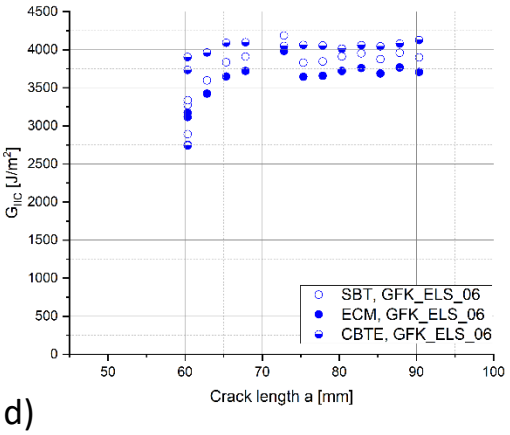


d)

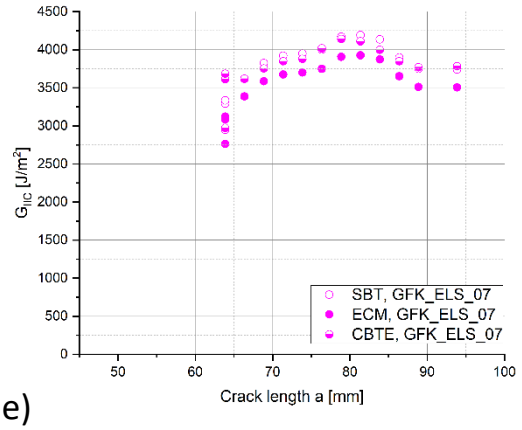


e)

Figure 7.2: a) Force-displacement curve and b)-e) R-curves of GFRP ELS tests according to ISO/DIS 15114 - 12 (cross-head speed = 0,5 mm/min).

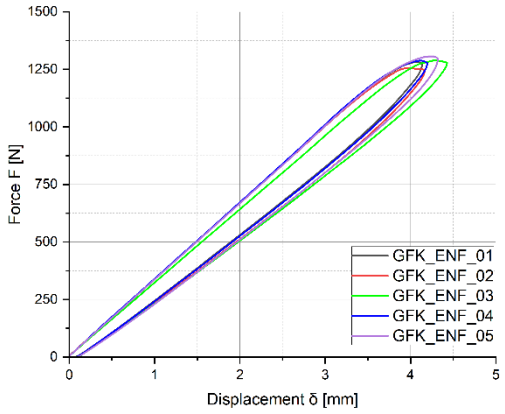


Figure 7.3: Force-displacement curve of GFRP DCB tests according to ASTM D7905 -14 (cross-head speed = 0,5 mm/min).

Table 7: Initiation results of GFRP ENF tests according to ASTM D7905 - 14 (cross-head speed = 0,5mm/min).

| | **AE [J/m²]** | **NL [J/m2]** | **Initiation of Propagation [J/m2]** |
|---|---|---|---|
| **GFK_ENF_01** | | 1960 | 2805 |
| **GFK_ENF_02** | 1378 | 1720 | 2285 |
| **GFK_ENF_03** | 1943 | 2287 | 2894 |
| **GFK_ENF_04** | 1754 | 1775 | 2525 |
| **GFK_ENF_05** | 1518 | 1996 | 2521 |

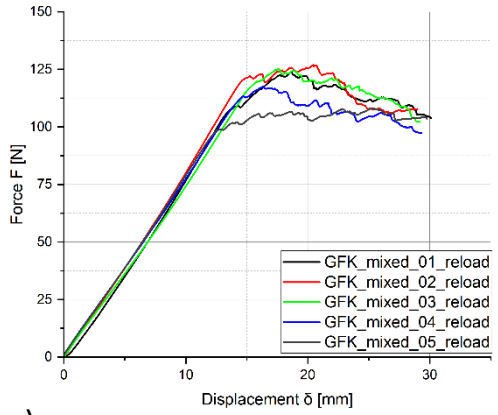


a)

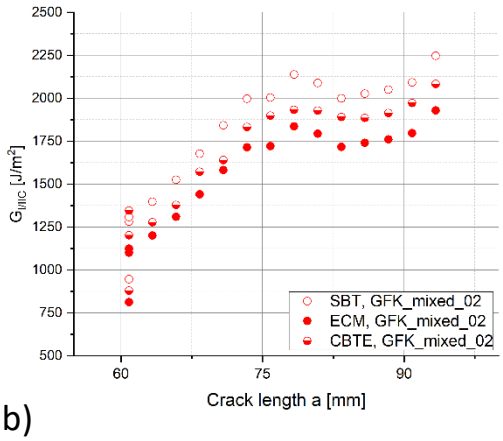


b)

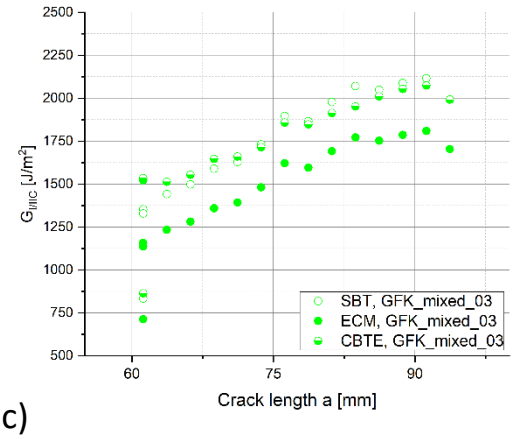


c)

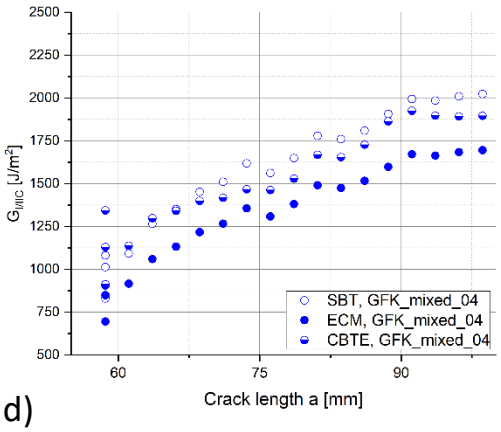


d)

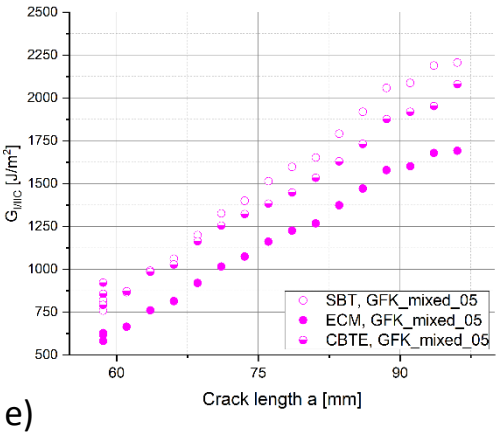


e)

Figure 7.4: a) Force-displacement curve and b)-e) R-curves of GFRP FRMM tests according to ESIS TC4 Protocol (cross-head speed = 1 mm/min).

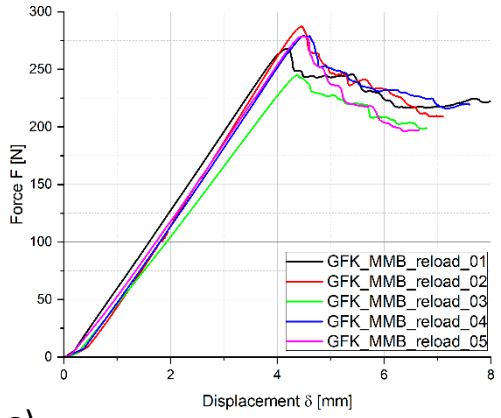


a)

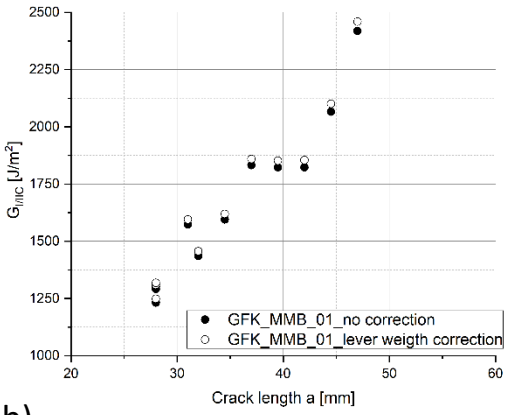


b)

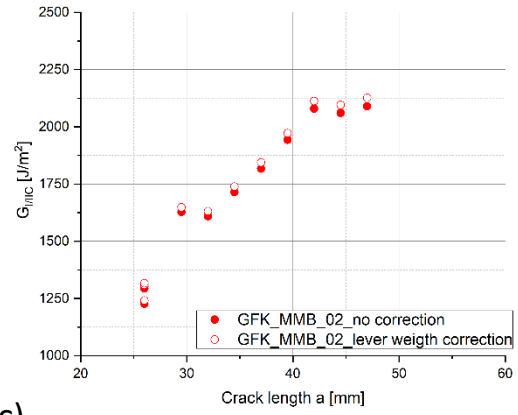


c)

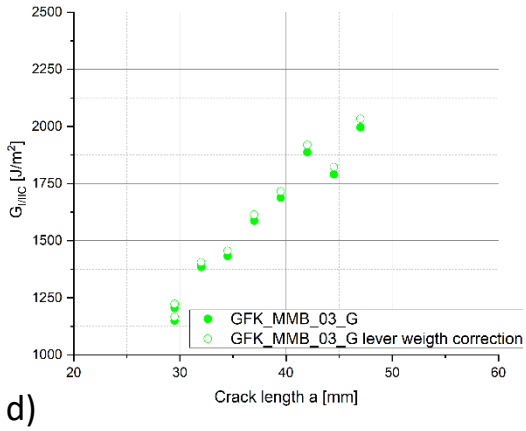


d)

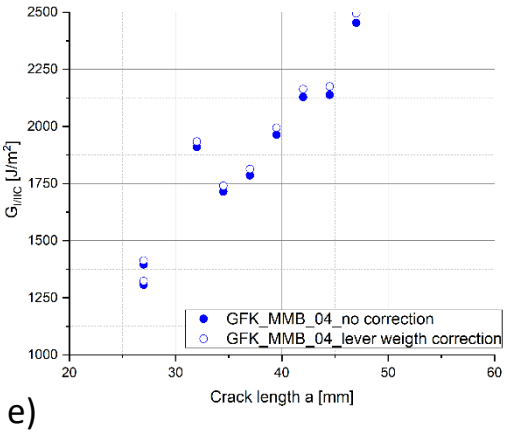


e)

Figure 7.5: a) Force-displacement curve and b)-e) R-curves of GFRP MMB tests according to ASTM D6671-13 (cross-head speed = 0,5 mm/min).

## 7.2 CFRP

Table 8: Overview of all CFRP results, obtained from average values of all calculation methods according to each norm.

| | | | AE [J/m²] | NL [J/m²] | VIS [J/m²] | 5 % / max [J/m²] | Propagation [J/m²] |
|---|---|---|---|---|---|---|---|
| **DCB** | **BT** | **Average** | 144,66 | 219,76 | 220,44 | 219,76 | 266,24 |
| | | **Deviation** | 20,56 | 33,37 | 31,89 | 33,37 | 41,89 |
| | **CBT** | **Average** | 132,83 | 201,08 | 201,76 | 201,08 | 251,28 |
| | | **Deviation** | 16,74 | 22,83 | 21,30 | 22,83 | 32,63 |
| | **MCC** | **Average** | 134,07 | 202,15 | 202,93 | 202,15 | 254,38 |
| | | **Deviation** | 12,01 | 14,89 | 13,07 | 14,89 | 28,08 |
| **ELS** | **SBT** | **Average** | 999,42 | 1014,53 | 1111,16 | 1476,50 | 1427,53 |
| | | **Deviation** | 110,45 | 92,38 | 144,04 | 531,19 | 107,46 |
| | **ECM** | **Average** | 685,04 | 743,27 | 805,74 | 1096,80 | 1043,96 |
| | | **Deviation** | 136,82 | 156,24 | 147,83 | 476,13 | 202,60 |
| | **CBTE** | **Average** | 855,93 | 939,17 | 1044,53 | 1285,15 | 1267,42 |
| | | **Deviation** | 32,52 | 82,45 | 37,80 | 184,46 | 68,13 |
| **ENF** | | **Average** | 1053,60 | 1129,40 | | | 1402,60[2] |
| | | **Deviation** | 172,29 | 111,04 | | | 120,30[2] |
| **FRMM** | **SBT** | **Average** | 387,29 | 504,99 | 612,45 | 642,77 | 860,19 |
| | | **Deviation** | 48,56 | 76,93 | 169,97 | 149,35 | 154,08 |
| | **ECM** | **Average** | 267,36 | 346,07 | 418,24 | 439,80 | 595,87 |
| | | **Deviation** | 42,72 | 47,92 | 96,67 | 84,08 | 127,92 |

[2] Initiation of propagation

| | | | | | | | |
|---|---|---|---|---|---|---|---|
| | **CBTE** | **Average** | 331,26 | 408,49 | 497,42 | 538,94 | 640,75 |
| | | **Deviation** | 33,78 | 38,10 | 79,82 | 81,12 | 82,34 |
| **MMB** | **No Corr.** | **Average** | 513,52 | 677,09 | 731,31 | 752,97 | 953,15 |
| | | **Deviation** | 103,24 | 89,76 | 82,39 | 98,92 | 104,72 |
| | **Lever weight Corr.** | **Average** | 527,77 | 693,62 | 748,46 | 770,37 | 962,69 |
| | | **Deviation** | 103,86 | 92,33 | 84,59 | 101,50 | 118,86 |

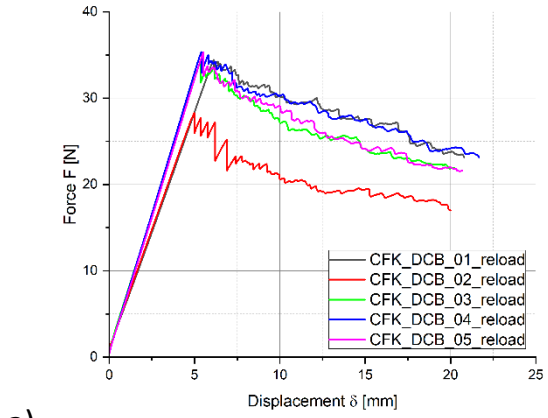


a)

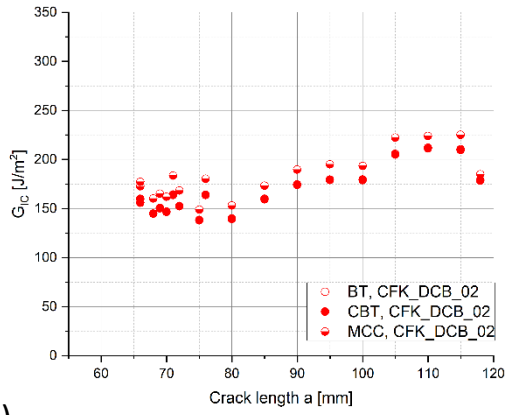


b)

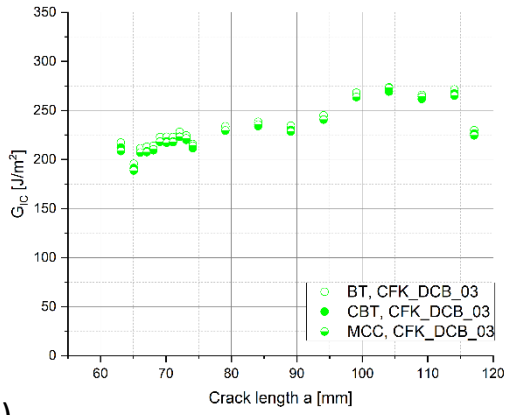


c)

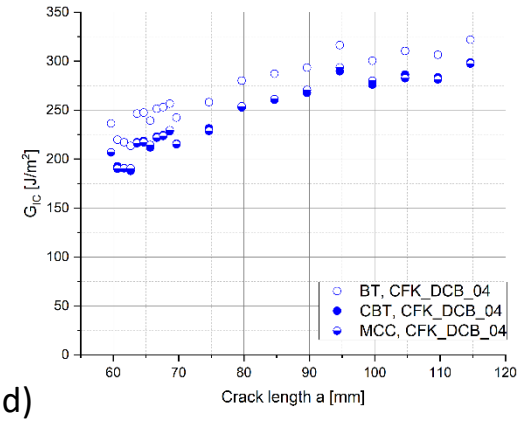


d)

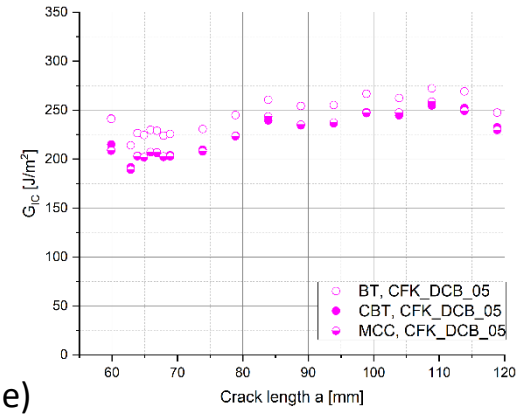


e)

Figure 7.6: a) Force-displacement curve and b)-e) R-curves of CFRP DCB tests according to ISO 15024 (cross-head speed = 1 mm/min).

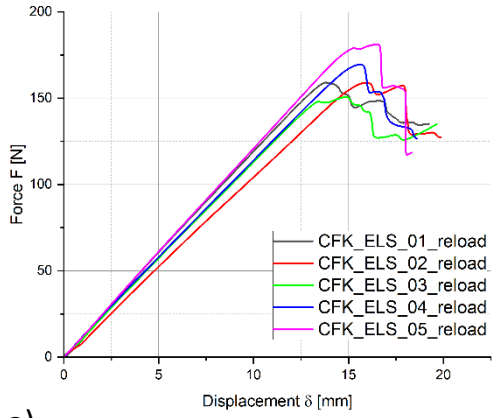


a)

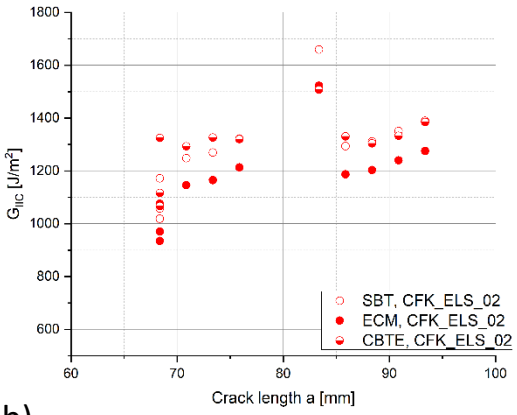


b)

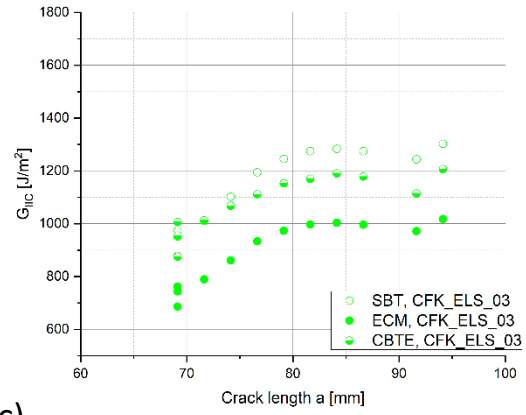


c)

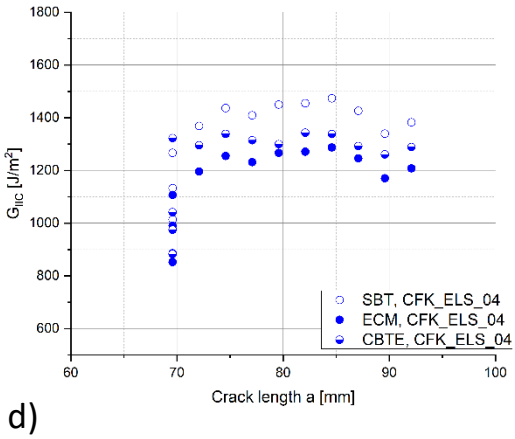


d)

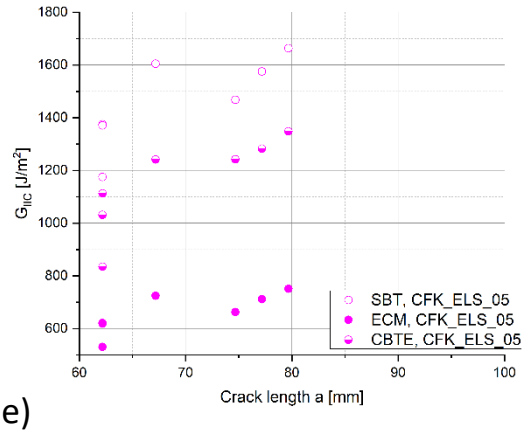


e)

Figure 7.7: a) Force-displacement curve and b)-e) R-curves of CFRP ELS tests according to ISO/DIS 15114 - 12 (cross-head speed = 0,5 mm/min).

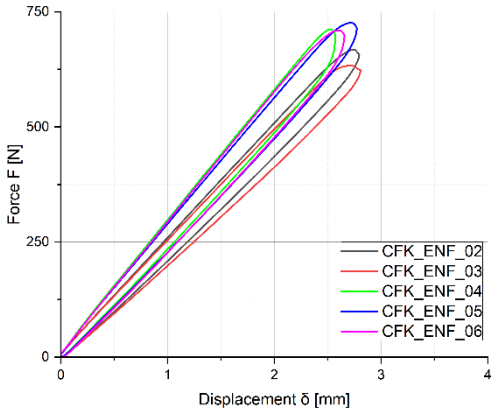


Figure 7.8: Force-displacement curve of CFRP DCB tests according to ASTM D7905 -14 (cross-head speed = 0,5 mm/min).

Table 9: Initiation results of CFRP ENF tests according to ASTM D7905 - 14 (cross-head speed = 0,5mm/min).

| | **AE [J/m²]** | **NL [J/m2]** | **Initiation of Propagation [J/m2]** |
|---|---|---|---|
| **CFK_ENF_02** | 831 | 1016 | 1269 |
| **CFK_ENF_03** | 1103 | 1112 | 1368 |
| **CFK_ENF_04** | 891 | 1324 | 1614 |
| **CFK_ENF_05** | 1304 | 1163 | 1443 |
| **CFK_ENF_06** | 1139 | 1032 | 1319 |

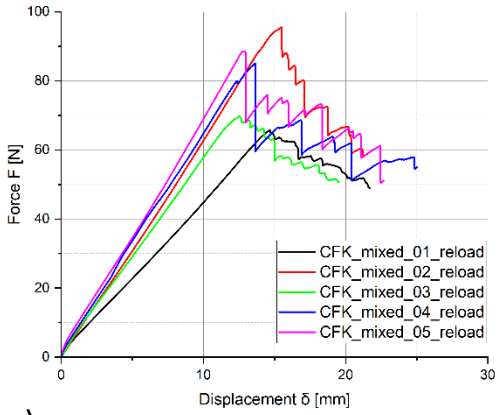


a)

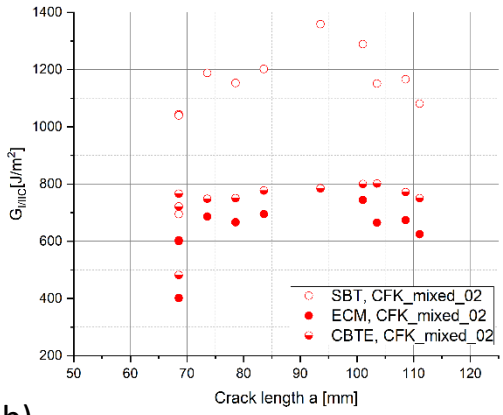


b)

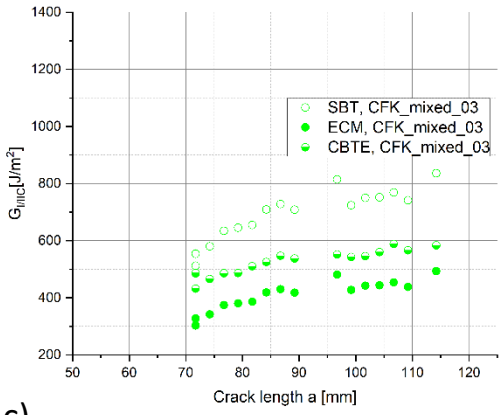


c)

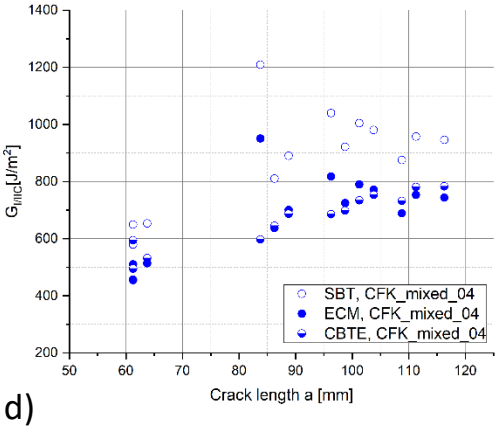


d)

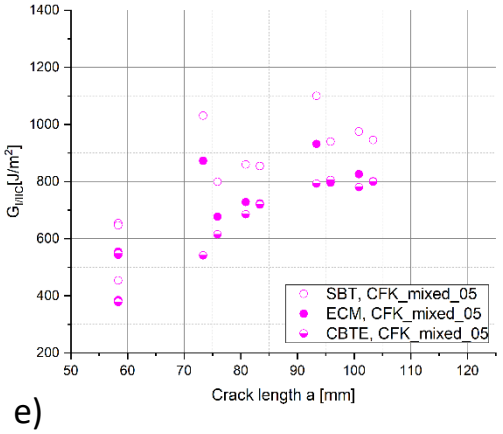


e)

Figure 7.9: a) Force-displacement curve and b)-e) R-curves of CFRP FRMM tests according to ESIS TC4 Protocol (cross-head speed = 1 mm/min).

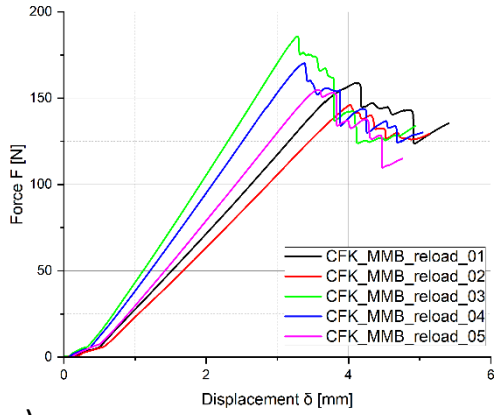


a)

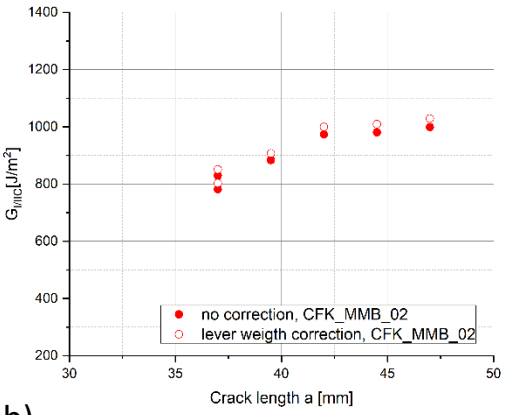


b)

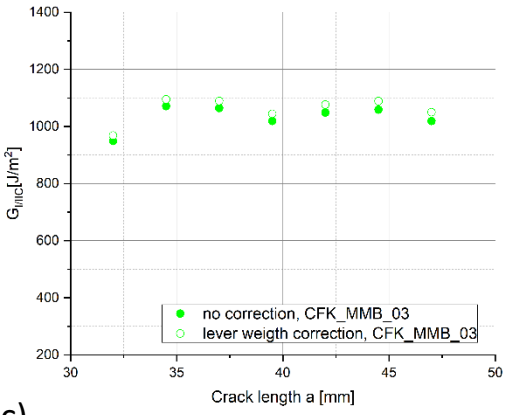


c)

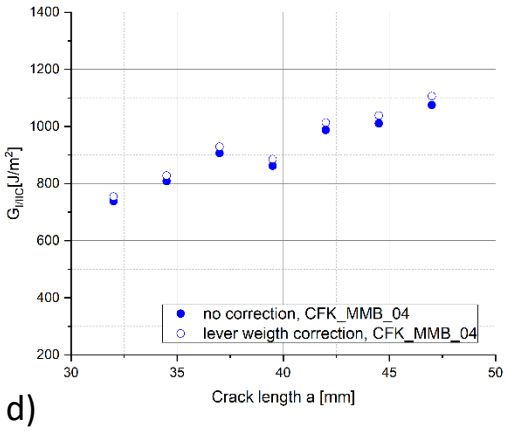


d)

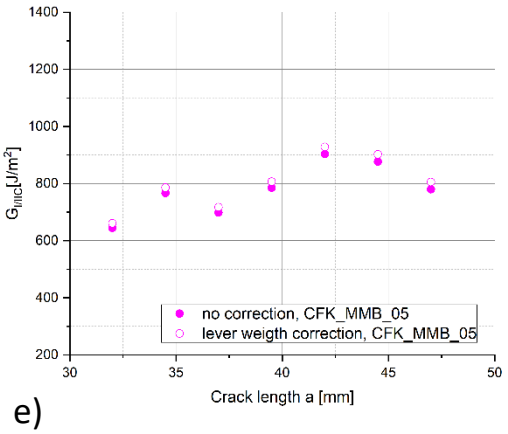


e)

Figure 7.10: a) Force-displacement curve and b)-e) R-curves of CFRP MMB tests according to ASTM D6671-13 (cross-head speed = 0,5 mm/min).